Dataset of Oil Slicks, Look-Alikes and Remarkable SAR Signatures Obtained from Sentinel-1 Data in the Eastern Mediterranean Sea

Yi-Jie Yang[1,2], Suman Singha[3,1], Ron Goldman[4], and Florian Schütte[5]

[1]Team SAR Oceanography, Remote Sensing Technology Institute, German Aerospace Center (DLR), Bremen, Germany
[2]Faculty of Mathematics and Natural Sciences, Kiel University, Kiel, Germany
[3]National Centre for Climate Research, Danish Meteorological Institute (DMI), Copenhagen, Denmark
[4]Israel Marine Data Center, Israel Oceanographic and Limnological Research (IOLR), Haifa, Israel
[5]GEOMAR Helmholtz Centre for Ocean Research Kiel, Kiel, Germany

Correspondence: Yi-Jie Yang (yi-jie.yang@dlr.de; yi-jie.yang@mailbox.org)

Abstract. Publicly available datasets for oil spill detection are scarce, making it difficult to compare the performance of different detection algorithms. To address this, this paper introduces a comprehensive labeled dataset of oil slicks, look-alikes, and other remarkable oceanic phenomena, derived from Sentinel-1 Synthetic Aperture Radar (SAR) products in the Eastern Mediterranean Sea in 2019. The dataset contains 3225 oil objects across 1365 image patches, along with an additional 2290 image patches featuring look-alikes or other phenomena. Data are available at https://doi.pangaea.de/10.1594/PANGAEA.980773 (Yang and Singha, 2025).

This dataset enables researchers to evaluate their oil spill detection models and compare performance with other studies. To facilitate this, the performance of an oil spill detector from a previous study on the dataset is provided as a baseline. In addition, to help the researchers better understand what phenomena their object detector might be confusing with oil slicks, the image patches without oil objects were sorted into several subgroups. On the other hand, for researchers looking to apply object detection models to oil slick detection but lacking a starting dataset, this dataset can serve as a valuable training resource. Beyond dataset presentation, this paper also explains the formation of different oceanic phenomena and their SAR signatures, supported by examples and supplementary materials. These insights help researchers from various backgrounds, such as remote sensing, oceanography, and machine learning, better understand the sources of SAR signatures.

1

Spaceborne Synthetic Aperture Radar (SAR) has been widely applied to marine oil pollution detection. While airborne systems play an important role in emergency response due to their flexibility in time of deployment and choice of sensors, with the advantage of wide coverage and the ability to observe at night and through clouds, spaceborne SAR can be used to monitor oil spills on a regular basis and provide early warning (Brown and Fingas, 2005; Brekke and Solberg, 2005). Oil slicks typically appear as dark formations in SAR imagery, but other phenomena can also manifest dark formations that look similar and are difficult to distinguish. Distinguishing oil slicks from these *look-alikes* has long been a challenge.

With the increasing computational capacity and the growing number of accessible SAR scenes since the launch of Sentinel-1 in 2014, many recent studies have used deep learning-based methods to detect oil spills and distinguish them from look-alikes. However, due to the lack of publicly available oil spill datasets, most studies had to collect their own oil spill dataset for model training. Some studies collected images of major accidents, such as the DeepWater Horizon incident, the Hebei Spirit oil tanker collision, and accidents reported in the local news, and cropped the acquired SAR images into multiple image patches (Chen and Wang, 2022; Hasimoto-Beltran et al., 2023; Mahmoud et al., 2023). These studies employed a limited number of SAR scenes, with less than 36 images, which means that the training dataset may not reflect the differences in radar backscatter between different acquisitions well. Other studies relied on either manual inspection by the authors (Topouzelis and Psyllos, 2012; Amri et al., 2022; Chen et al., 2023) or local collaboration with other institutions or services (Konik and Bradtke, 2016; Cantorna et al., 2019; Zeng and Wang, 2020). These studies focused on the development of new oil spill detection models, but the use of different datasets made it difficult to compare the performance of different studies.

Recognizing the challenges posed by the absence of a comprehensive dataset, Krestenitis et al. (2019) published an oil spill detection dataset. It contains approximately 1000 Sentinel-1 SAR images with their corresponding ground truth masks, indicating five classes: oil spill, look-alikes, land, ship, and sea areas. The oil spills were reported by the European Maritime Safety Agency (EMSA) through the CleanSeaNet service. However, it is not openly available, the proposal is required to obtain the dataset. On the other hand, a recent work has contributed its training dataset to Zenodo, an open repository for datasets (Trujillo-Acatitla et al., 2024). The dataset includes oil spills reported by the National Oceanic and Atmospheric Administration (NOAA) and EMSA CleanSeaNet. There are 2850 image patches, half with oil spills inside, half without oil spills but with background or look-alikes inside. These two datasets offer pixel-wise classification of the images. However, in low-wind conditions or in areas where there are frequent look-alikes, there may be large areas of dark formations. For this reason, previous studies have proposed a two-step approach with coarse detection of oil slicks over a large area and refinement of the results to a pixel-wise level (Nieto-Hidalgo et al., 2018; Yang et al., 2024). This approach can theoretically increase efficiency, as the final detection is only performed if there are detections in the first step, and may therefore be helpful for a near real-time (NRT) monitoring system. Therefore, the dataset presented in this paper provides an object-based annotation of the oil spills, which aims to support research that follows the idea of this approach.

There are many different sources of look-alikes, such as low-wind areas, internal waves, ~~mixing and vertical advection in the ocean~~upwelling, and biogenic films, that modify the ocean surface and introduce signatures in SAR imagery. It is important to understand which types of look-alikes the model cannot distinguish well, but this information is not available in previous datasets. Therefore, the published dataset includes image patches of oil slicks and other prominent marine signatures, stored in *oil set* and *no-oil set*, respectively. For the image patches in *no-oil set*, the K-Means unsupervised clustering algorithm was used to further sort the patches into several subgroups to help users better understand the performance of their algorithms on different sources of look-alikes. Note that K-Means categorizes each image as a whole under a specific cluster. In other words, unlike oil slicks in the *oil set*, which were labeled as objects, no annotation is attached to image patches in the *no-oil set*.

In addition, previous datasets used the reports from the existing service, but in many areas such services are not available. There is a lack of clear guidance on how to distinguish between different phenomena and what data can be used to support

them. This paper gives examples of different phenomena and explains how SAR signatures are manifested and how they can be interpreted with the help of other supplementary materials.

This published dataset focuses on the Eastern Mediterranean Sea, which is one of the marine oil pollution hotspots due to its heavy maritime traffic (Carpenter and Kostianoy, 2016). There are 1365 image patches with 3225 oil objects in *oil set* and 2990 image patches in *no-oil set*. Sect. 2 provides an overview of the dataset, including the spatial distribution of the data, the preprocessing steps applied to the SAR scenes, the procedures used to collect the dataset, and the sources of supplementary material used to understand the dark formations. Sect. 3 describes in detail how the oil slicks were annotated and the concept of the K-Means clustering algorithm used to classify the image patches.

The dataset and this paper can be used for different purposes. For researchers wishing to start in an area where there are no existing services for the recording of oil spills (i.e. no ground truth oil spills available), Sect. 4 can be used as a reference as it explains how oil slicks and different oceanic or atmospheric conditions contribute to SAR signatures. For studies that already have their own object detector for oil slicks, this dataset can be used as a separate dataset to test their model performance. Subsect. 5.1 provides an evaluation of the performance of an object detector used in an NRT automated oil spill detection system developed in Yang et al. (2024). In addition, the clustered *no-oil set* can provide an indication of how to improve the model. Furthermore, the dataset can be used as a training dataset by researchers who are just starting to apply object detection algorithms to oil spill detection applications. Although the dataset only covers oil spills in the Eastern Mediterranean Sea, a previous study showed that with such a locally focused oil object detector, only a small additional dataset is needed to extend the use of the detector to another region (Yang and Schnupfhagn, 2025). Additional technical information in the Subsect. 5.2 should be read before using the dataset. Section. 6 summarizes how this data descriptor and dataset can be used and add value to the community.

2 Materials

This section contains information about the dataset and has the following structure: Subsect. 2.1 lists general information about the SAR products and explains the corrections applied to them. Subsect. 2.2 gives an overview of the dataset and explains the procedures for preparing this dataset. Subsect. 2.3 shows a collection of different supplementary data that could help inspect dark formations. Note that all the time stamps shown in this paper and the dataset are in UTC. The map boundaries in figures were derived from Wessel and Smith (1996).

2.1 Sentinel-1 Data

Sentinel-1 SAR Level-1 Ground Range Detected (GRD) products were obtained from the Copernicus Open Access Hub, which provided data through the end of October 2023. The Copernicus Data Space Ecosystem operates as an improved and updated version of it and provides Earth observation data and services, including tools, graphical interfaces, and Application Programming Interfaces (APIs).

The dataset covers Sentinel-1A and Sentinel-1B products, which share the same orbit plane with a 180 orbital phasing difference; the repeat cycle was six days. Note that Sentinel-1B stopped delivering data since 23 December 2021. Sentinel-1 products from 2019 covering the Eastern Mediterranean Sea were acquired and preprocessed. The acquisitions from ascending and descending orbits in the area were taken at around 15:30–16:05 and 03:30–04:05, respectively. Those scenes are in Interferometric Wide Swath (IW) acquisition mode with a swath width of 250 km, and the incidence angle ranges between 29.1 and 46.0. In this area, dual-polarization VV-VH products were provided. The data in cross-polarization mode (i.e., VH or HV) generally exhibit lower backscattering and, therefore, are influenced more by background and instrument noise compared to those in co-polarization mode (i.e., VV or HH) (Woodhouse, 2006). For this reason, only VV-polarized products were collected in the dataset.

A series of corrections, border noise removal, thermal noise removal, and calibration were applied to the SAR products. The continuous products were assembled and multilooked with a factor of 2. The final backscattering coefficient, σ^0, is given in decibels (dB). These preprocessing steps were done with the help of the Sentinel Application Platform (SNAP) Graph Processing Framework (GPF) (European Space Agency, 2020). Note that the data were preprocessed with SNAP version 8, and certain circular patterns were produced at regions with relatively low backscattering in a few images; Figure 1 shows such an example from 27 August 2019. Therefore, some image patches collected in the dataset also contain such artifacts (see Figure 2). As they should not be the bottleneck of the detection algorithm, these image patches are kept in the dataset.

Afterwards, the preprocessed data were normalized to 0–255, for training the object detector. The normalized image, I_N, ~~is~~ was calculated by the sigmoid function:

$$I_N = \frac{255}{1 + e^{\frac{-(I-\beta)}{\alpha}}}, \tag{1}$$

where I is the original image value. In this study, β and α equal to the median and three times the standard deviation ($3 \cdot \sigma$), respectively, of the original image values in the corresponding preprocessed data. There is no specific function that should be applied for image normalization. The parameters used to generate the dataset were determined by the authors through trial and error, as they provide good contrast between oil slicks and their surroundings according to human eyes. The object detectors shown in Subsect. 5.1 were trained using image patches for which a different image normalization method, provided by the Geospatial Data Abstraction Library (GDAL), was applied. Therefore, different image normalization methods may not be the key factor in the poor performance of the object detection algorithms. A previous study rescaled the image with maximum value equals to mean plus three times the standard deviation (Karathanassi et al., 2006).

2.2 Dataset

The published dataset utilized the annotation of oil objects in the framework of our previous study (Yang et al., 2024), where all preprocessed Sentinel-1 data covering the Southeastern Mediterranean Sea in 2019 were inspected jointly by two human interpreters. Only the dark formations agreed upon by both interpreters as oil slicks were given labels. Image patches including these labeled oil objects were generated and stored in the *oil set*. However, without ground truth oil spills available, the labeled

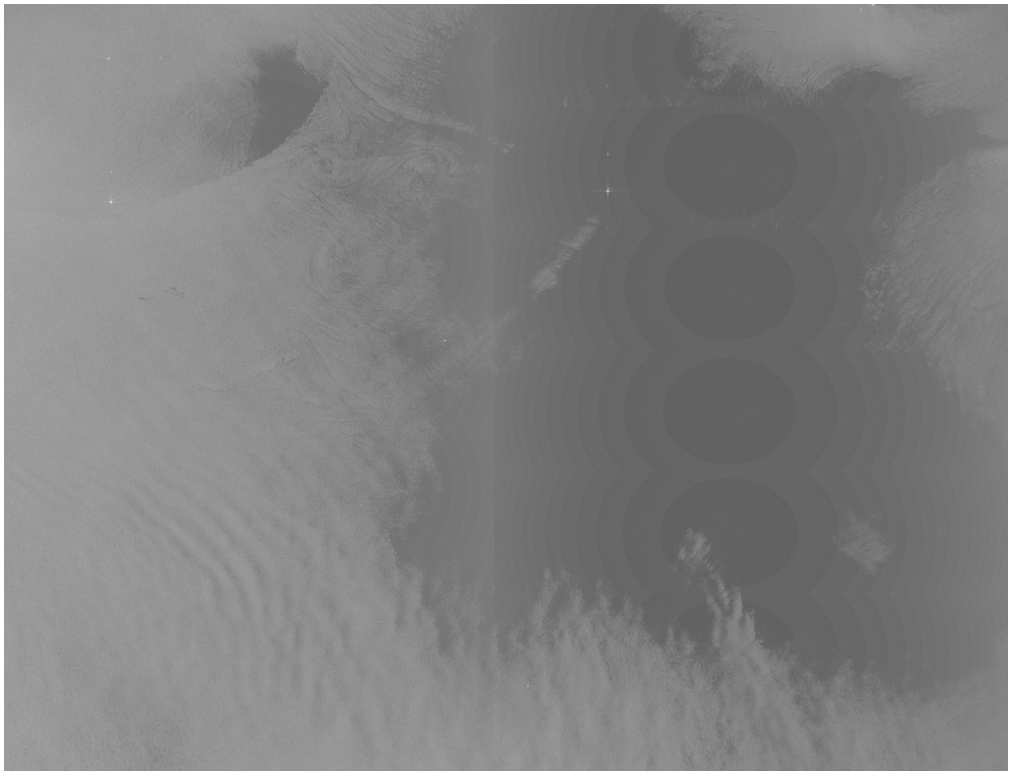

Figure 1. Preprocessed data with certain artifact produced after applying thermal noise removal in SNAP version 8. Note that the figure ~~is obtained from~~ contains modified Copernicus Sentinel ~~Data~~data [2019].

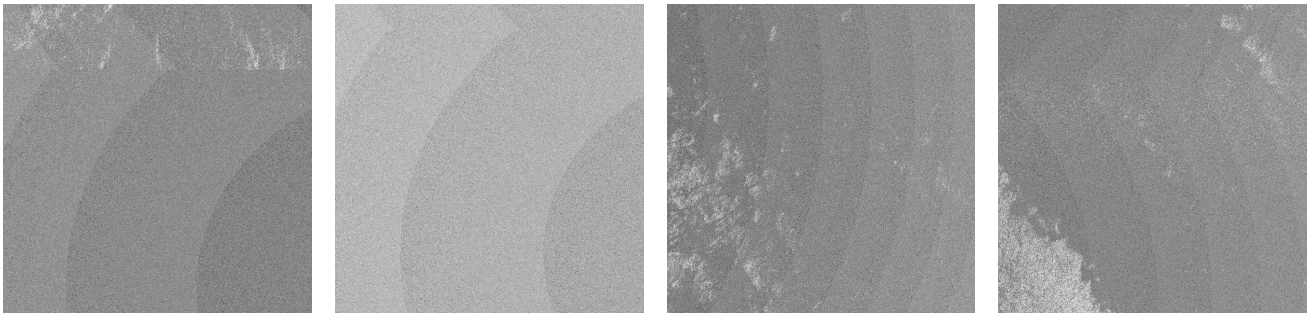

Figure 2. Image patches in the dataset with artifact as shown in Figure 1. The tags for these image patches (from left to right) for referring to their information in the provided data table are nw-0603-03-000100, nw-0609-03-000106, nw-0547-03-000044, and nw-0553-03-000050 (see also Subsect. 2.2 and Appendix A). The figure contains modified Copernicus Sentinel data [2019].

120 oil objects might not only belong to oil spills but also to other possible chemical spills. A successful oil spill detection system should be able to distinguish oil slicks from look-alikes; therefore, it is essential to take into account the image patches without

oil slicks in them. In addition to the *oil set*, the published dataset also includes a *no-oil set*, which provides image patches without oil slicks but with look-alikes or other remarkable SAR signatures present.

Sources of pollution and other phenomena could differ between coastal and offshore areas. Hence, depending on whether the image patch covers land areas or not, image patches in the *oil* and *no-oil sets* are further split into *coast* and *water* subsets. The structure of the different subsets can be understood as follows:

```
oil/
    coast/
    water/
no_oil/
    coast/
    water/
```

To efficiently collect image patches for the *no-oil set*, an object detector, custom-trained with oil objects but lacking images with look-alikes, was employed to target dark formations in the collected SAR scenes. These detections were compared to the locations of the inspected oil slicks, and those that have no intersection with the oil objects were regarded as look-alikes and stored in the *no-oil set*.

To include look-alikes from different sources equally, these image patches were categorized by the K-Means unsupervised clustering algorithm (see Subsect. 3.2 for algorithm explanations). The *water* and *coast* subsets were first separated with the help of a land mask, and then they were clustered into 12 and 5 subgroups, respectively. Afterwards, 2100 and 500 image patches were randomly chosen from the two subsets, respectively. As offshore regions are of more interest, more image patches from the *water* subset were kept in the dataset. Each cluster contains a similar number of selected image patches compared to the other cluster from the same subset. Figure 3 shows the numbers of image patches in each cluster; the red vertical lines show the number of image patches being randomly picked. It should be noted that one image patch might have dark formations from more than one source due to the complex manifestation of oceanographic phenomena on SAR imagery. Each subgroup should not be regarded as look-alikes from one specific source; the users should only consider the categories as a reference to help comprehend what kinds of SAR signatures are likely to be misinterpreted by their algorithms.

Sect. 4 provides explanations for SAR signatures from different ocean phenomena. The dataset includes image patches in JPG format, and the corresponding annotations are in Pascal VOC XML format (Everingham et al., 2010). Figure 4 shows the heatmap of image patches in the *oil* and *no-oil sets*. The oil spill inspection area is defined from 34.7 N to the south and 36 E to the east until the coastline and marked as a blue boundary in the figure. However, all the Sentinel-1 SAR products from 2019 covering the area in longitude from 30 E to 36 E and in latitude from 31 N to 34.7 N were automatically examined while collecting image patches for the *no-oil set*. As the oil inspection area is smaller than the distribution extent of the image patches in the *no-oil set*, these image patches were manually inspected, and the ones with oil ~~spills~~ slicks or unknown and unsure dark formations were removed from the dataset to avoid confusion. Table 1 gives the final statistics of the published dataset. Information about image patches in the dataset is recorded in a data table in Excel format; different subsets are recorded

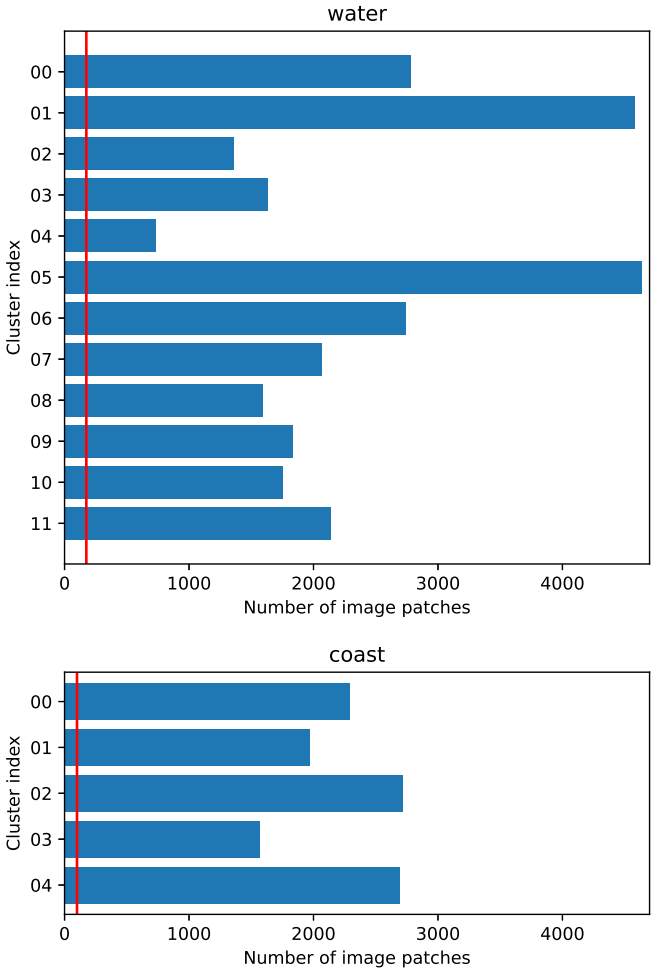

Figure 3. Numbers of image patches in different clusters by K-Mean algorithm. The vertical red lines indicate the number of image patches randomly selected from the subsets. These image patches were then manually inspected, and the number of image patches in the final published dataset from each subgroup is presented in Table 1.

in separate sheets. Appendix A provides an extracted data table recording the information of image patches displayed in this article. For users who would like to preprocess SAR products themselves, Sentinel-1 product IDs and the corner coordinates of the image patches are provided. The data table includes the following fields relating to image patches:

- patch name,
- Sentinel-1 product start and stop date time,
- Sentinel-1 product ID,

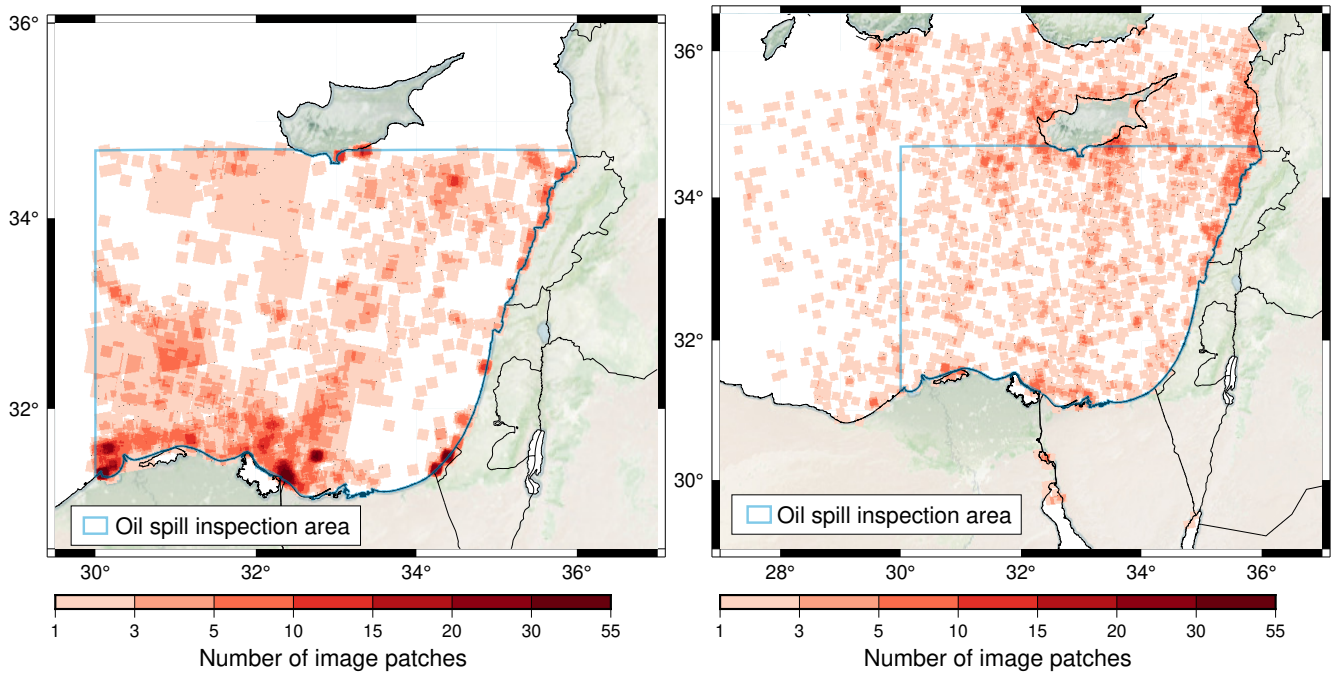

(a) *oil set* (b) *no-oil set*

Figure 4. Heatmap of the image patches in the (a) *oil* and (b) *no-oil sets*. The base map was obtained from Stevens (2020), and the coastlines and borders were obtained from Wessel and Smith (1996).

- dimension of the image patch in pixels,
- corner coordinates of the image patch in longitude and latitude (WGS84).

The patch name follows the naming convention:

`MM_YYYYMMDD_HHMMSS_HHMMSS_PP_i`

where `MM` refers to satellite mission, in this dataset, all the data are from Sentinel-1 mission, `S1`; `YYYYMMDD` shows the date of the product and `HHMMSS` shows the start and stop time of the product; `PP` indicates the polarization mode (e.g., VV); `i` is a series of numbers assigned when generated the image patches.

In the preprocessing step, continuous SAR products were assembled. Therefore, image patches might be located at the overlapping areas of the two products; in this case, both Sentinel-1 product IDs would be listed in the data table. The dimension of the image patch is default to 640×640 px, which is the same as the model input size for our object detector; but to keep the original shapes of some large oil slicks, there are a few image patches that have dimensions greater than the default. In this case, the object detector would rescale these image patches, but oil slicks should still be detectable.

The tie points grids in Sentinel-1 products provide the geolocation information in WGS84 geocentric coordinate system. To calculate the geolocation of the four corner points, upper left (ul), upper right (ur), bottom right (br), and bottom left (bl), of

Table 1. Statistics of the *oil set* and *no-oil set*.

Dataset	*oil set*		*no-oil set*			
Subset	*water*	*coast*	*water*		*coast*	
Number of image patches	990	375	00	172	00	76
			01	171	01	84
			02	160	02	75
			03	162	03	44
			04	81	04	72
			05	166		
			06	166		
			07	171		
			08	175		
			09	168		
			10	174		
			11	173		
				1939		351
Number of oil objects	2284	941	N/A		N/A	

N/A: not applicable

each image patch, its surrounding tie points were loaded, and the corner coordinates were estimated by the least squares fitting. The same procedure was used to obtain the object coordinates in *oil set*. For the *oil set*, additional fields for oil objects are provided:

- corner coordinates of the oil objects in longitude and latitude (WGS84),
- image coordinates of the oil objects referred to their corresponding image patch,
- the size (in pixels) of the bounding box annotating the oil object.

The data tables for *oil set* are sorted by objects; that is, if there are four oil objects in one image patch, there will be four separate rows for the four oil objects, and they should have the exactly same image patch information, such as patch name, Sentinel-1 product ID, and geolocation of the image patch. On the other hand, as there is no object in the *no-oil set*, each row refers to the information of its corresponding image patch. On top of all the fields explained earlier, each row in the table is referred to a unique tag with one image tag and an additional object tag or cluster tag.

The image tag is a two-letter subset tag followed by four-digit image serial number. The first letter of the subset tag is either o or *n*, referring to *oil set* and *no-oil set*, respectively; the second letter, *w* or *c*, stands for the subset *water* or *coast*. The image serial number is a sequence of numbers starting from 0001 for each subset, ordered by patch names.

In the *oil set*, each object gets an object tag with a two-digit object index and a six-digit object serial number. The object index numbers the objects in each image patch, counting from 01; the object serial number is a sequence of objects for all the objects in one subset, counting from 000001. As an example, ow-0795-01-001867 is a tag with an image tag ow-0795 and an object tag 01-001867, meaning that the object is the first object in the 795th image patch and the 1867th object in the *ow* subset.

To follow the same tag format, a cluster tag with two-digit cluster index and a six-digit cluster patch serial number is assigned to each image patch in the *no-oil set*. The cluster index refers to the class assigned by K-Means clustering methods, with 12 and 5 classes for *nw* and *nc* subsets, respectively; the index counts from 00. The cluster patch serial number is a sequence of image patches for all the image patches in one class, counting from 000001. Take nc-0308-04-000029 as an example, the image tag nc-0308 shows that this is the 308th image patch in the *nc* subset and the cluster tag tells that this is the 29th image patch in the 04 class.

The patch name was assigned when the image patch was generated; it contains information about the date and time of the acquisition. Since the data publisher prefers a dataset without folders, the tags are used as filenames and the folders have been removed. However, users are encouraged to rename the filenames to the patch names if they prefer. However, it should be noted that image patches from the *oil* and *no-oil* sets were generated separately, so in some rare cases the image patches may have the same names. Therefore, it is recommended to create a folder structure as explained at the beginning of this subsection.

2.3 Supplementary Data

Dark formations in SAR imagery can be caused by oil spills or look-alikes. Deliberate oil spills are mainly associated with human activities, such as offshore oil operations and oil transport. Some existing services, such as the Global Oil and Gas Extraction Tracker (GOGEC) and the European Marine Observation and Data Network (EMODnet), provide locations of oil, gas and offshore installations. These services can help to identify areas with a high potential for platform spillage. On the other hand, look-alikes can be related to a variety of oceanic, atmospheric, and geological factors that modulate the roughness of the sea surface. Supplementary materials may be used to help in cross-comparison to better comprehend the sources of dark formations. Table 2 directs the reader to various services that the authors found valuable in explaining SAR signatures or that are used in the examples shown in Sect. 2.1.

Ocean information such as wind speed, waves, sea surface temperature (SST), and chlorophyll *a* (chl-*a*) concentration can be obtained from satellite, model, and in-situ data. The Ocean Virtual Laboratory (OVL) portal, funded by the European Space Agency (ESA), provides a quick and broad overview of ocean monitoring through its visualization tool. Additional information such as SAR roughness and bathymetry is also available. The other service, the Copernicus Marine Data Store (MDS) from the E.U. Copernicus Marine Service Information (CMEMS; acronym derived from its former name, Copernicus Marine Environment Monitoring Service), is an ocean data catalog with products at global and regional scales. Similar to the

Table 2. Platforms for supplementary data.

Platform	url	Reference
Ocean Virtual Laboratory (OVL) portal	https://ovl.oceandatalab.com/	
Copernicus Marine Data Store (MDS)	https://data.marine.copernicus.eu/	
• Mediterranean Sea - High Resolution and Ultra High Resolution L3S Sea Surface Temperature	https://doi.org/10.48670/moi-00171	CMEMS (a)
• Mediterranean Sea, Bio-Geo-Chemical, L3, daily Satellite Observations (1997–ongoing)	https://doi.org/10.48670/moi-00299	CMEMS (b)
• Global Ocean Hourly Sea Surface Wind and Stress from Scatterometer and Model	https://doi.org/10.48670/moi-00305	CMEMS (c)
Copernicus Climate Data Store (CDS)	https://cds.climate.copernicus.eu/	
Israel Meteorological Service	https://ims.gov.il/en	Ministry of Transport and Road Safety, Israel
General Bathymetric Chart of the Oceans	https://www.gebco.net/	GEBCO (2023)

OVL portal, MDS provides MyOcean Viewer, which allows users to add different products to the map viewer. Moreover, the dataset can be easily retrieved with commands using the Copernicus Marine Toolbox.

Another Copernicus service, the Climate Data Store (CDS), provides climate data such as global precipitation data; this service is implemented by the European Centre for Medium-Range Weather Forecasts (ECMWF). However, the rainfall data used in this article were obtained from the coastal weather stations obtained from the Israel Meteorological Service, provided by the Ministry of Transport and Road Safety, Israel. The service provides daily rainfall and rainfall automated recorded every 10 minutes. Note that these systems tend to underestimate the rainfall in major events according to the information provided by the service.

The General Bathymetric Chart of the Oceans (GEBCO) has released several global bathymetric and topography grids with a spatial resolution of 15 arc seconds since 2003. This model is especially useful for providing context to SAR data in areas with varying bathymetry, which can affect the interpretation of ocean surface roughness in satellite imagery.

Sect. 4 explains different SAR signatures and provides examples of explanations on different dark formations with the help of the supplementary data. A summary list for those examples along with the supplementary data is provided in Subsect. 4.9 (see Table 3). Note that not all the data in the dataset were confirmed with the supplementary data but with the experience of the human inspectors and their understanding of the study area.

3 Methods

3.1 Manual Inspection

As stated in Subsect. 2.2, the annotations were initially done in the framework of our previous study (Yang et al., 2024) with the help of an open source image annotation tool, LabelImg (Tzutalin, 2015). Those image patches were geolocated, as in this case, referring to other supplementary materials and understanding the location of the spills is easier. However, the image patches and the oil objects in the published dataset were provided in the range and azimuth direction of the corresponding SAR products.

Continuous oil spillage from one source can be like multiple oil slicks after the physical processes. Therefore, definitions of those oil objects might be tricky; one can interpret them as one oil object or several oil objects. In addition, the extent of an oil slick might not be easy to define; for example, the evaporation of oil could make it look like it is fading away in SAR scenes. It shall be noted that different definitions of the extent of one oil object can play a vital role in model performance calculations. For example, if there is one oil object in the dataset, but the object detector considers it to be two nearby objects, they may be considered false positives if they do not pass the threshold used to define true positives (see Subsect. 5.1 for performance evaluation). Figure 5 provides some image patches inside the published dataset with oil object labels to illustrate how the authors annotated the oil slicks. The tags of these image patches are provided as captions, and the explanations for tags are shown in Subsect. 2.2; readers can find an extracted data table in Appendix A.

3.2 K-Means Clustering

K-Means (Lloyd, 1982; MacQueen, 1967) is an unsupervised algorithm to partition a set of observations into a specific number, k, of clusters. The concept is to obtain k clusters by satisfying that the sum of the distance between each observation and the mean vector (centroid) of its corresponding cluster is minimum; the Euclidean distance is a common way of calculating such distance. To achieve this idea, the algorithm first randomly partitions observations into k sets and calculates their centroids. Based on these centroids, each observation is assigned to its nearest cluster. Afterwards, the algorithm iteratively updates the centroid and assign observations of each cluster to a new cluster until convergence is achieved.

In image clustering, each image is represented as a feature vector in the vector space that contains the features of the image, such as texture and shape. To extract features of the image patches in the *no-oil set*, the InceptionV3 model (Szegedy et al., 2015) pre-trained with a large visual database, ImageNet (Deng et al., 2009), was used. K-Means clustering was then applied to categorize the image patches with the help of the Scikit-learn K-Means module. Figure 6 shows examples of image patches from each cluster (see Appendix A for the patch information).

The purpose of using the K-Means clustering method is to provide a *no-oil set* in which the signatures of different phenomena appear more balanced. In other words, the clustering method categorized the dataset, and then the same number of image patches from each class were randomly selected. However, for better understanding the performance of the object detector on different kinds of SAR signatures, it would be ideal if all image patches within each class have similar sources of phenomena

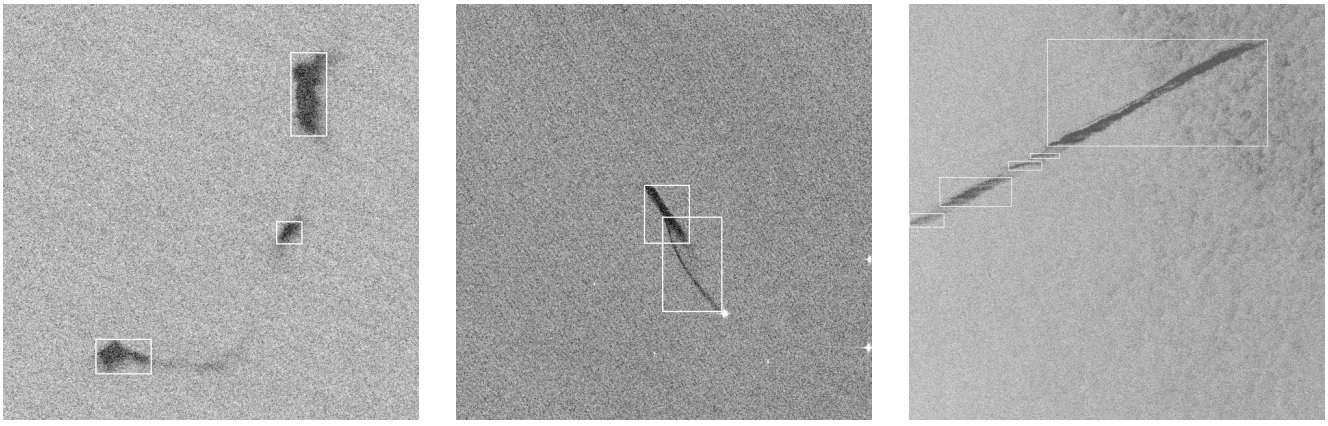

(a) ow-0267 (b) ow-0276 (c) ow-0438

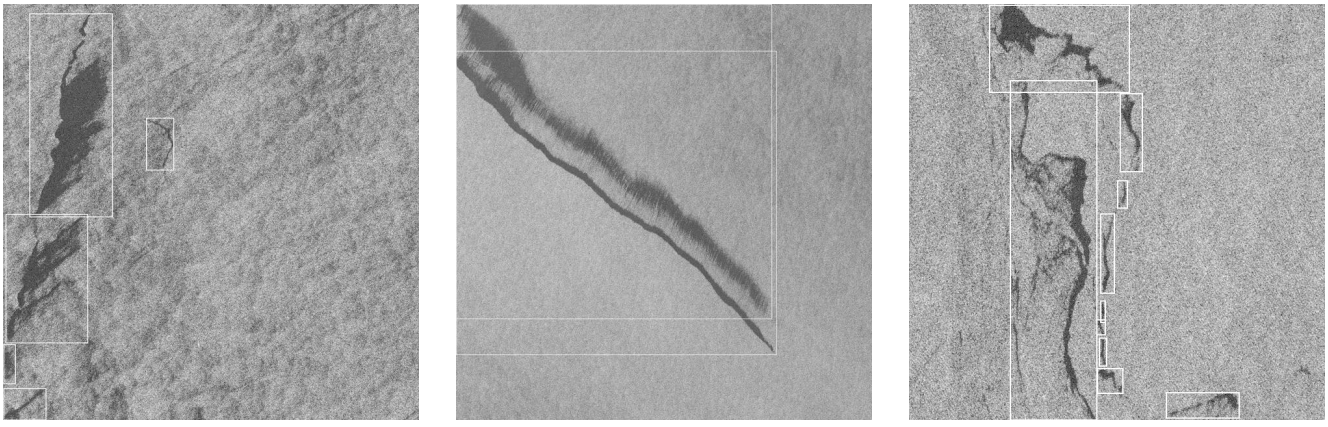

(d) ow-0447 (e) ow-0463 (f) ow-0643

Figure 5. Image patches from the published dataset along with the labels of the oil objects marked with white bounding boxes. Their corresponding image tags (explained in Subsect. 2.2) are also provided as captions, the readers can find their further information recorded in the data table (see Appendix A). The figure contains modified Copernicus Sentinel data [2019].

that could be explained by humans. Therefore, human interpretation was considered when selecting the number of classes, which was adjusted by reviewing image patches in different classes.

Sea states in coastal areas are often complicated by factors such as bathymetry and interaction with land. However, open water typically experiences larger-scale dynamics that can manifest a variety of different SAR signatures. Therefore, the offshore subset is expected to have a greater variety of sources of SAR signatures. Thus, the K-means clustering method was given 12 and 5 classes for the *nw* and *nc* subsets, respectively.

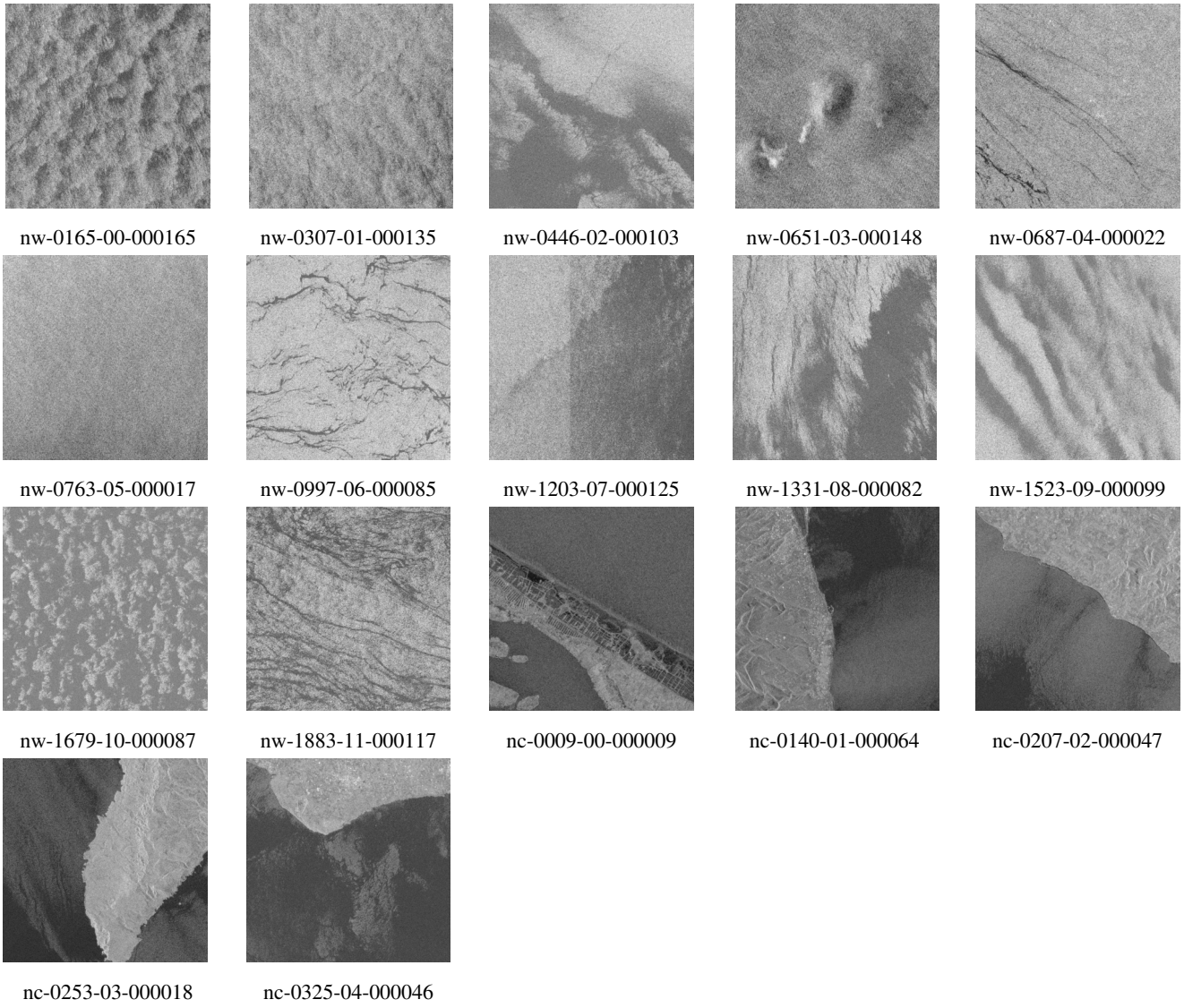

Figure 6. Image patches from different clusters in the *no-oil set*. Their corresponding tags (explained in Subsect. 2.2) are also provided as captions, the readers can find their further information recorded in the data table (see Appendix A). The figure contains modified Copernicus Sentinel data [2019].

4 SAR Signatures

The radar transmits microwave pulses and some of them are reflected back to the radar, the normalized power of the received signals over the actual ground area is known as radar backscatter, σ^0. The radar backscatter depends on radar system characteristics (e.g., polarization, wavelength, and radar geometry) and the properties of the target (e.g., shape, dielectric constant, and roughness) (Woodhouse, 2006).

For ocean applications, sea surface roughness is generally regarded as a key factor; variations in surface roughness are closely related to wind speed and direction (Robinson, 2004; Woodhouse, 2006). Winds form friction between air and water and cause small capillary waves in millimeter-to-centimeter scales. These wind-induced capillary waves are usually regular over a large area and act as resonant Bragg scatterers, which can interfere constructively if the Bragg condition is satisfied as defined:

$$2d \cdot \sin\theta = n\lambda, \tag{2}$$

where d is the spacing of the scatterers, θ is the incidence angle, λ is the radar wavelength, and n is an integer. The spacing of the scatters can be regarded as ocean wavelength. The incidence angle of Sentinel-1 IW mode ranges between 29.1 and 46.0; therefore, according to the equation, the resonant ocean wavelength is at a similar scale as radar wavelength. In addition, the waves should travel along the range direction (either parallel or anti-parallel) to obtain the strongest resonance. This constructive interference is also known as resonant Bragg scattering or the coherence scattering mechanism. On the other hand, if the condition is not fulfilled, destructive interference occurs, and the scattered power is reduced.

The ocean surface contains small-scale capillary waves, gravity waves in meter scales, swell, and large-scale currents; therefore, the ocean surface is considered a complicated summation of a wave spectrum of different wavelengths. However, the radar returns come from these short capillary waves, which have wavelengths similar to the radar wavelengths, rather than the longer waves; hence the Bragg mechanism is often used to interpret radar backscatter at the ocean surface (Robinson, 2004).

The following subsections illustrate and explain SAR signatures due to oil slicks, different oceanic or atmospheric phenomena, or human-related activities. Some supporting materials listed in Table 2 are used to comprehend the phenomena and to better interpret the SAR signatures. If users need more detailed information about the supporting data, they should check the descriptions in Sect. 2.3 or refer to the websites in Table 2. Note that these examples are not provided in the published dataset. The published dataset only includes image patches from 2019; however, the examples are not limited to the time interval. The selections are mainly based on the accessibility of the supplementary materials and are to avoid SAR signatures due to multiple phenomena, which make it challenging to interpret. These examples are not cropped into image patches as most phenomena influence an area larger than the size of an image patch. In addition, instead of displaying them in SAR geometry in range and azimuth, they were projected to the World Geodetic System 1984 (WGS84), making it easier to compare them with different supplementary data. All the example scenes are listed at the end of this section (Subsect. 4.9), so that users can download SAR scenes themselves from the Copernicus Data Space Ecosystem.

4.1 Oil slicks

The presence of oil slicks decreases the surface tension of the water and lowers wind friction; therefore, short gravity and capillary waves are dampened, which reduces the radar backscatter and results in dark formation in SAR imagery. Spaceborne SAR sensors can observe a large area on a regular basis; however, to investigate the quantity, type, and thickness of the oil, it usually requires multiple sensors, such as infrared, ultraviolet, microwave radiometer, and laser fluorosensors (Ferraro et al.,

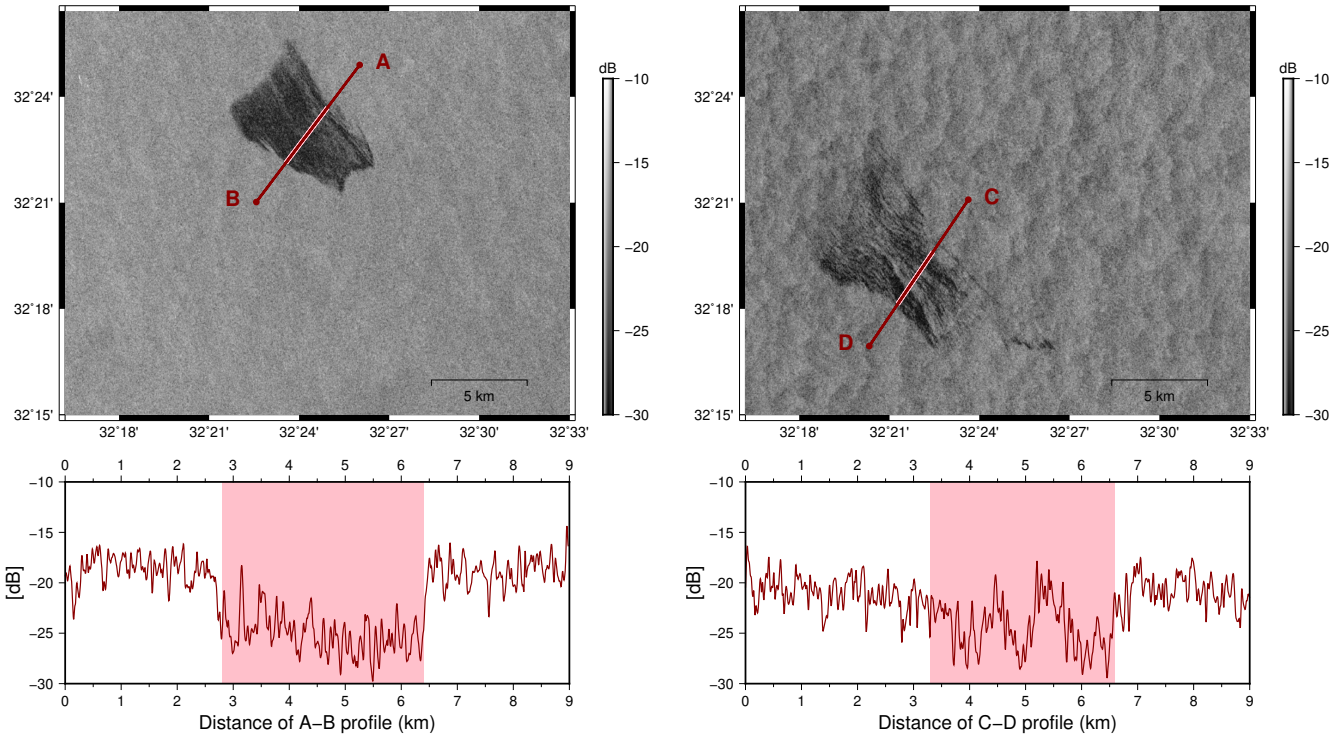

(a) 2022-11-03 15:49

(b) 2022-11-04 03:52

Figure 7. Examples of an oil slick appearing in SAR acquisitions around 12 hours apart, showing its changes overtime. The profiles illustrate the radar backscatter along the red line, and the shadowed area highlights approximately where the oil-induced dark formation is located. The figure contains modified Copernicus Sentinel data [2022].

2009; Fingas and Brown, 2017). This dataset was inspected without data from other sensors available; therefore, the distinction between oil spills and other possible chemical spills is not clearly defined.

Figure 7 shows SAR scenes covering an oil slick in two separate acquisitions taken at 15:49 on 3 November 2022 and at 03:52 on 4 November 2022. Separate charts show the profiles of radar backscatter sampled along the red lines, the shadowed areas mark the approximate locations of oil-induced dark formations. Wind speeds at 16:00 on 3 November 2022 and 04:00 on 4 November 2022 were acquired from CMEMS (c); the corresponding average wind speeds of the shown area were ~~3.94 m s^{-1} and 3.90 m s^{-1}~~3.94 m s^{-1} and 3.90 m s^{-1}, both blowing in the southeastward direction. The first acquisition shows an oil slick with apparent differences in backscattering compared to its surrounding areas. Though the wind conditions seemed similar, the two acquisitions had different heading and look angles; therefore, the wind-induced signatures differed and resulted in lower overall backscattering in the second acquisition. This example illustrates the dynamicity of an oil spill over time in SAR data and how oil properties, ambient wind speed and direction relative to the SAR azimuth make oil slicks appear differently in SAR data.

Reports or records are usually not provided for smaller deliberate oil discharges, meaning that there is no ground truth; thus, inspecting oil slicks should carefully consider the possibilities of dark formations from other phenomena. The following subsections introduce those *look-alikes* and provide supplementary materials to better understand the signatures.

4.2 Wind

As explained at the beginning of this section, wind is closely related to the sea surface roughness, which is a key element for SAR signatures. Under low winds, the sea surface is smooth and calm, and the backscattering will be close to the SAR noise floor; therefore, the modulation of backscattering from oil slicks can not be revealed. On the other hand, if the sea surface is too rough under high winds, oil slicks are also not possible to be indicated. Previous studies suggested optimal wind speed ranges between 2–~~3 m s^{-1}~~ 3 m s^{-1} and 7–~~12 m s^{-1}~~ 12 m s^{-1} for oil slick detection using SAR (Gade et al., 2000; Robinson, 2004; Brekke and Solberg, 2005). As the visibility of oil slicks depends on not only SAR sensors but also the age and type of the oil, the upper and lower limits differ in different studies; this range should be considered a hint. Oil slicks can still be observed outside this range in some circumstances.

Some atmospheric phenomena can influence ocean surface roughness and result in certain SAR signatures; examples of these phenomena are the atmospheric front, phenomena related to geographic features, unstable atmospheric boundary layer (ABL), and atmospheric gravity waves (AGWs, also known as atmospheric internal waves) (Robinson, 2004). Since AGWs form similar patterns as oceanic internal waves (OIWs), they are both explained in Subsect. 4.3.

Sudden changes in wind speed and direction can create an atmospheric front that separates two air masses and is shown as a boundary between weaker and stronger radar backscatter. Similar signatures of the fronts can also be seen where winds blow from land to sea through coastal terrain. The land usually cools down during the night, but the temperature over the adjacent sea may remain, in which case the air pressure over the land would be higher than that over the sea, resulting in the wind blowing offshore. This cooler and denser air from the land rolls out to the sea and pushes the warm air over the sea upwards, creating a cold land breeze front (Robinson, 2004). Land breeze fronts usually create near-shore bands of modulated surface roughness parallel to the coast, as shown in Figure 8. Similarly, during the night, the cool air mass from the mountains could flow down the valley driven by the density flow; this is known as the katabatic wind. If the mountains are located in coastal areas, the winds would blow toward the sea and spread out in a fan shape, as shown in Figure 9 (a). Figure 9 (b) indicates the topography with mountains and valleys close to the shore in Lebanon; the terrain and bathymetry model is obtained from GEBCO (2023). These katabatic wind-induced signatures tend to reoccur at roughly the same places since they are related to the topography (Robinson, 2004). Note that the bright pixels are especially distinct at the bottom part of Figure 9 (a) was due to radio frequency interference (RFI), which will be explained in Subsect. 4.8.

Figures 8 and 9 (a) were both taken at about 03:44 UTC, which should be 06:44 local time (UTC+3, considering daylight saving time); shortly after sunrise at about 06:03 and 06:29 local time, respectively. Land breeze and katabatic winds usually occur during the night, when the land has cooled down a lot, and before the air warms up during the day. Based on our experience inspecting SAR images in this area, the katabitic wind fronts are commonly observed in SAR images in the

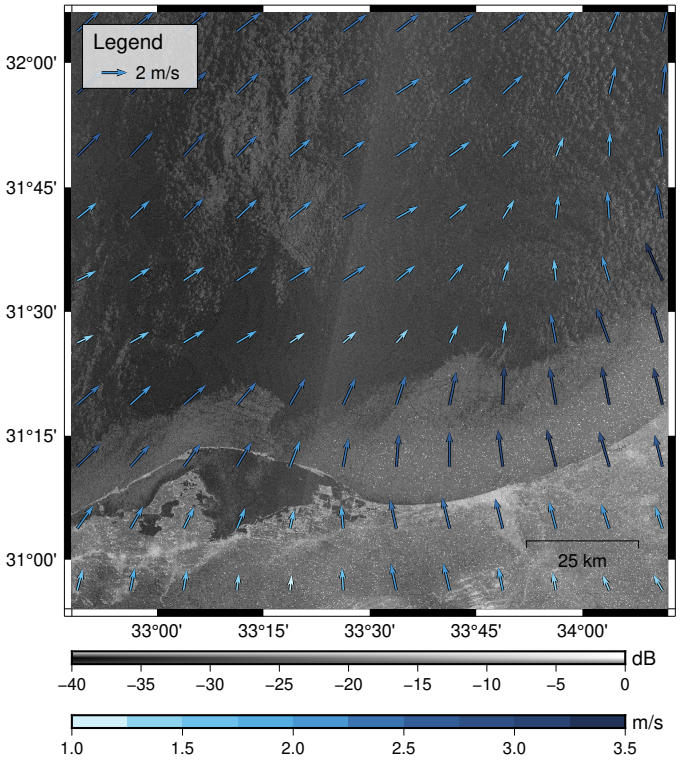

Figure 8. An example of land breeze fronts in the SAR scenes taken at 03:44 on 2 August 2023 near Egypt, plotted with the simulated wind speed at 04:00 obtain from CMEMS (c). The figure contains modified Copernicus Sentinel data [2023]. The plotted coastline was obtained from Wessel and Smith (1996).

descending orbit (taken at around 03:45 UTC) covering the coastal areas of Lebanon and Israel. In addition, wind shelters and wind shadows can also appear as low radar backscatter along the coast or off an island.

Dynamics in the ABL driven by surface wind can increase surface roughness and lead to phenomena seen in SAR imagery. When the air is heated by a warmer sea surface, it expands and becomes less dense than the air above it. The resulting ABL instability drives convective cells in which warm and humid air rises in updrafts and is replaced by descending cooler air. The downflow of the cold air induces a radial outflow; coupled with the wind flow, they lead to the fluctuations of surface roughness and form cellular patterns in SAR images (Robinson, 2004); such patterns can be observed in Figures 8 and 9 (a).

~~The unstable stratification and convective~~ Thermodynamic instability in ABL, ~~such as cold air outbreak over the sea~~mainly determined by temperature and humidity, can lead to ~~the occurrence of~~ wind streaks forming streak-like patterns in SAR (Zhou et al., 2025). These wind streaks enable the estimation of wind direction by using SAR (Lehner et al., 1998). Similar streak patterns may also result from the intersection of wind-driven surface currents and Stoke's drift of surface waves. This intersection can lead to Langmuir circulation, producing helical roll vortices ~~, which~~ that are approximately parallel to the wind direction (Langmuir, 1938; Etling and Brown, 1993). These helical rolls appear alternatively as the right and left helices, resulting in upward

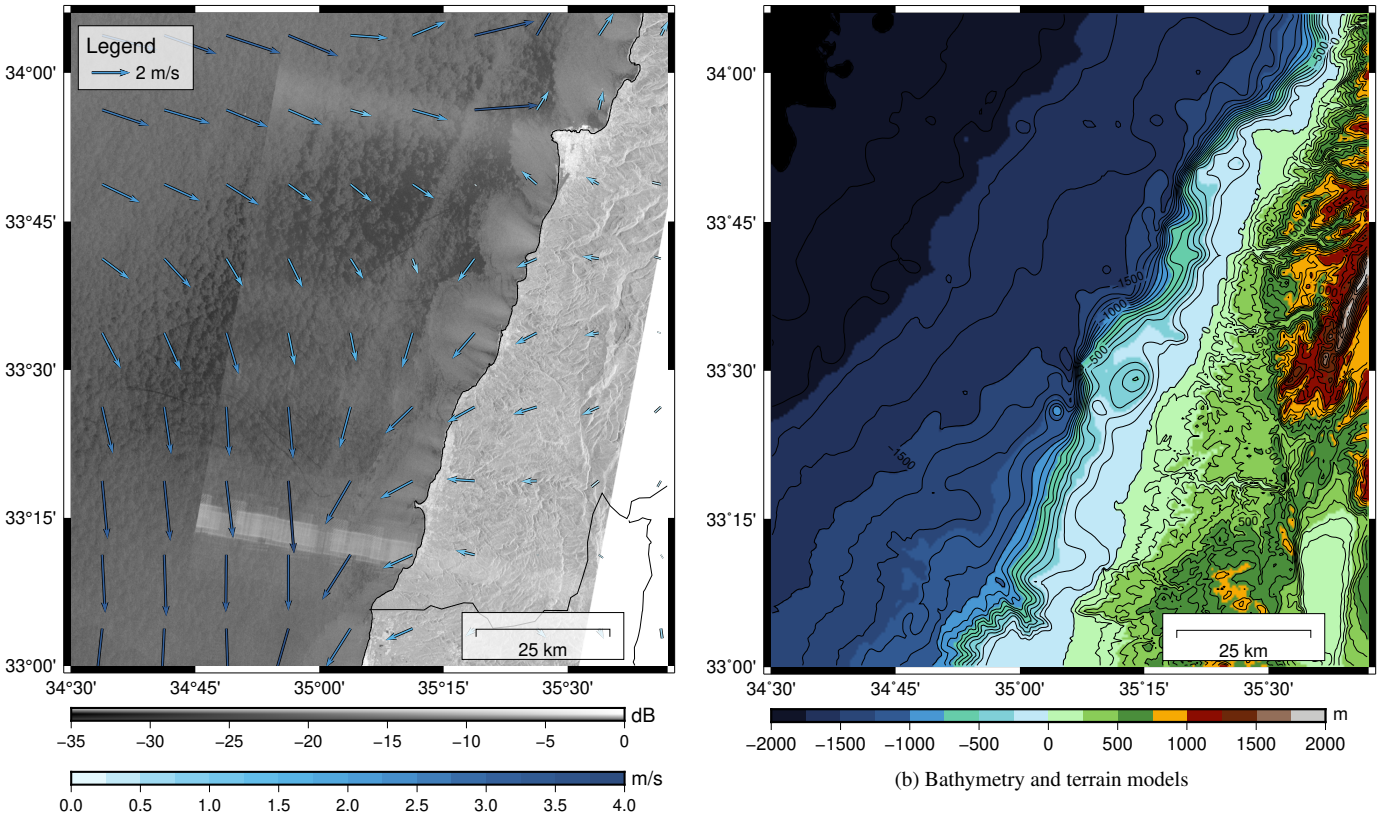

(a) Sentinel-1 SAR

(b) Bathymetry and terrain models

Figure 9. An example of katabatic wind-induced signatures in the SAR scenes taken at 03:43 on 24 September 2022 near Lebanon, plotted with the simulated wind speed at 04:00 obtain from CMEMS (c). The left figure contains modified Copernicus Sentinel data [2022]. The coastline and borders were obtained from Wessel and Smith (1996).

and downward flows between the rolls, which lead to higher and lower surface roughness and are shown as dark and bright streaks in SAR (Langmuir, 1938; Robinson, 2004). ~~These wind streaks enable the estimation of wind direction by using SAR (Lehner et al., 1998).~~ Figure 10 ~~presents such wind streaks that are aligned well with the wind~~ shows an example of such streak patterns alongside the wind speed and direction.

4.3 Internal Waves in the Ocean and Atmosphere

Internal waves can occur in any stratified medium, such as fluids with varying density. In the ocean and atmosphere, two restoring forces act on internal waves: gravity and the Coriolis force. Thus, perturbations of the vertical density gradient will generate internal waves with frequencies between the Brunt-Vñisñlñ frequency and the Coriolis parameter.

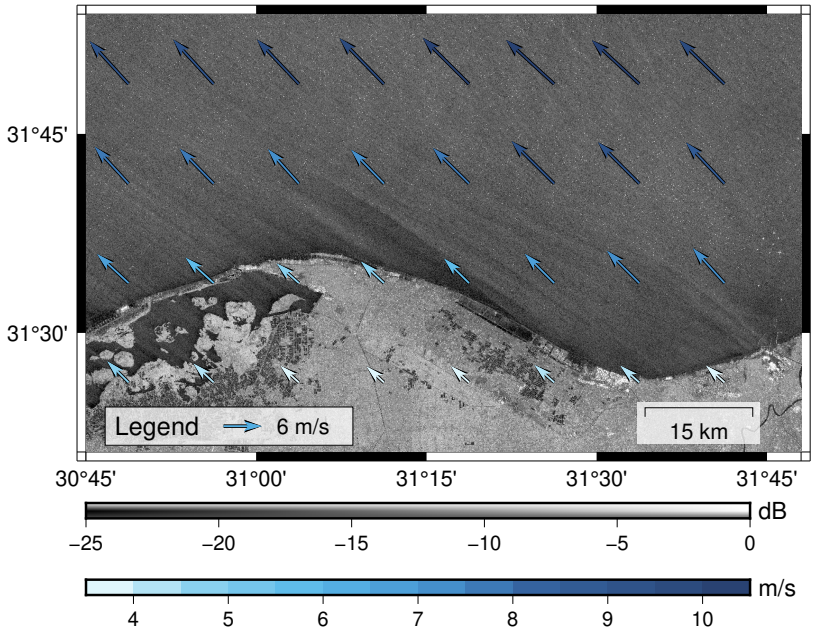

Figure 10. An example of ~~wind streaks~~ streak patterns in the SAR scene taken at 03:52 on 27 January 2023 near Egypt, plotted with the simulated wind speed at 04:00 obtain from CMEMS (c). The figure contains modified Copernicus Sentinel data [2023].

The primary drivers of internal waves in the ocean are tides, closely followed by the wind. The particle motion of the oceanic internal waves (OIWs) produces surface convergence and divergence that modulate the short gravity and capillary waves, resulting in amplification and attenuation of these waves, respectively. As a result, the alternating convergence and divergence zones on the sea surface lead to patterns of bright and dark strips in SAR imagery (Alpers et al., 2008; Robinson, 2010; Alpers and Huang, 2011). Similar to the ocean, disturbances in atmospheric stratification also generate internal waves, often referred to as atmospheric gravity waves (AGWs).

When for example external forces push the air upward, the air gets cooler, and the water vapor saturation point is likely to be reached, which leads to the formation of clouds. On the other hand, when the air gets warmer, water evaporates, resulting in a clear sky. Therefore, when the moisture content of the air is sufficient and the amplitude of the AGW is large enough, cloud streets and clear skies are expected to appear over the crests and troughs of the AGW, respectively. The variations of wind stress at the sea surface disturb the small surface roughness and result in dark and bright strips in SAR scenes, similar to OIW (Alpers and Huang, 2011).

Internal waves play a crucial role in energy transport within the ocean and atmosphere. The interactions of internal waves with itself, topography and other ocean or atmosphere dynamics are highly complex and not yet fully understood. Through the SAR images and the identification and clustering of possible OIW and AGW signatures by the algorithm, there is now a high number of images available, providing a better spatial and temporal resolution of the internal wave field and allowing for a deeper understanding of these processes. However, it can be challenging to distinguish between OIWs and AGWs

in general and within the presented dataset. Nevertheless, the shape and structure of the wave patterns provide hints for their differentiation (Alpers and Huang, 2011), as summarized in the following. In general, OIWs are observed in low-wind areas since otherwise their SAR signatures are too weak to be detected, especially in conditions with wind speeds greater than ~~10 m s^{-1}~~10 m s^{-1}; contrastingly, AGWs can be observed at all wind speeds. In addition, OIWs mostly appear near an upwelling area or at locations where rough topography, shallow underwater ridges, sea mounts, or steep shelves are present. On the other hand, AGWs usually appear in areas where wind interacts with mountain ranges, different air masses collide, strong wind shear occurs, or convective activities are associated with cold fronts (e.g., thunderstorms). ~~In the following, an example of an OIW and an AGW is presented, along with hints on how to best distinguish between them.~~

A previous study presented OIWs propagating from the edge of the continental shelf and supported their explanation with temperature, salinity, and density profiles from a CTD probe (Liu et al., 1998). Figure 11 shows the SAR scenes taken at 15:41 on 28 March 2024 at the coast of Lebanon, plotted with the contour of bathymetry and terrain model obtained from ~~GEBOC~~GEBCO (2023). The bathymetry profile along the red line is shown in a separate chart. ~~According to the hourly sea surface wind velocity from scatterometer and model at 16:00 on 28 March 2024 obtained from MDS (CMEMS, c), the wind speed in this area was around 0.14 m s^{-1} to 1.28 m s^{-1} with an average of 0.51 m s^{-1}, which is a possible condition for OIWs to generate patterns in SAR scenes. Additionally, the slope bathymetry~~ Dark and bright strips can be seen east of the continental slope (between points B and ~~C in Figure 11 reveals the probable cause of the OIWs~~A). The strips appear to be parallel to the both the coastline and the continental slope. Therefore, the ~~dark and bright strips in Figure 11 are more likely due to OIWs than AGWs. Examples of SAR images containing OIWs with similar causes, propagating from the edge of the continental shelf, can also be found for example in Liu et al. (1998).~~ stripes me be due to oceanic internal waves generated in the interaction between currents and the slope, or due atmosperic internal waves generated as lee waves from the mountain topography. Without additional data, such as vertical profiles of ocean and atmosphere, it is difficult to determine the sources of internal waves in this example.

Figure 12 shows the SAR scenes taken at 03:52 on 27 May 2023 and a separate profile of radar backscattering along the red line. On top of the SAR scene, the hourly sea surface wind at 04:00 on 24 May 2023 obtained from the scatterometer and model (CMEMS, c) is plotted; the wind speed in this area was around ~~7.13 m s^{-1} to 11.09 m s^{-1}~~2.87 m s^{-1} to 10.18 m s^{-1}, and the average wind speed was ~~9.24 m s^{-1}~~7.97 m s^{-1}. The higher the wind speed, the less likely it is to be OIWs; therefore, the strip patterns are more likely to come from AGWs. Based on the consecutive scenes taken before (i.e., northern to) the shown scene, the wave patterns cover large ocean areas, which are commonly observed in SAR scenes with AGWs (Li, 2004). In addition, streaks from AGWs are usually approximately perpendicular to the direction of the wind (Robinson, 2004; Li, 2004) and are expected to show up as narrow dark bands followed by broad bright bands alternatively (Alpers and Huang, 2011).

4.4 Areas of mixing and vertical advection in the ocean

In the ocean, there are a variety of processes that can lead to mixing or vertical advection, especially near shallow topography or the coast. In the deeper layers of the ocean, more nutrients and colder water can be found compared to the upper layers. This means that mixing or vertical advection typically results in a colder sea surface and a vertical nutrient flux, which in

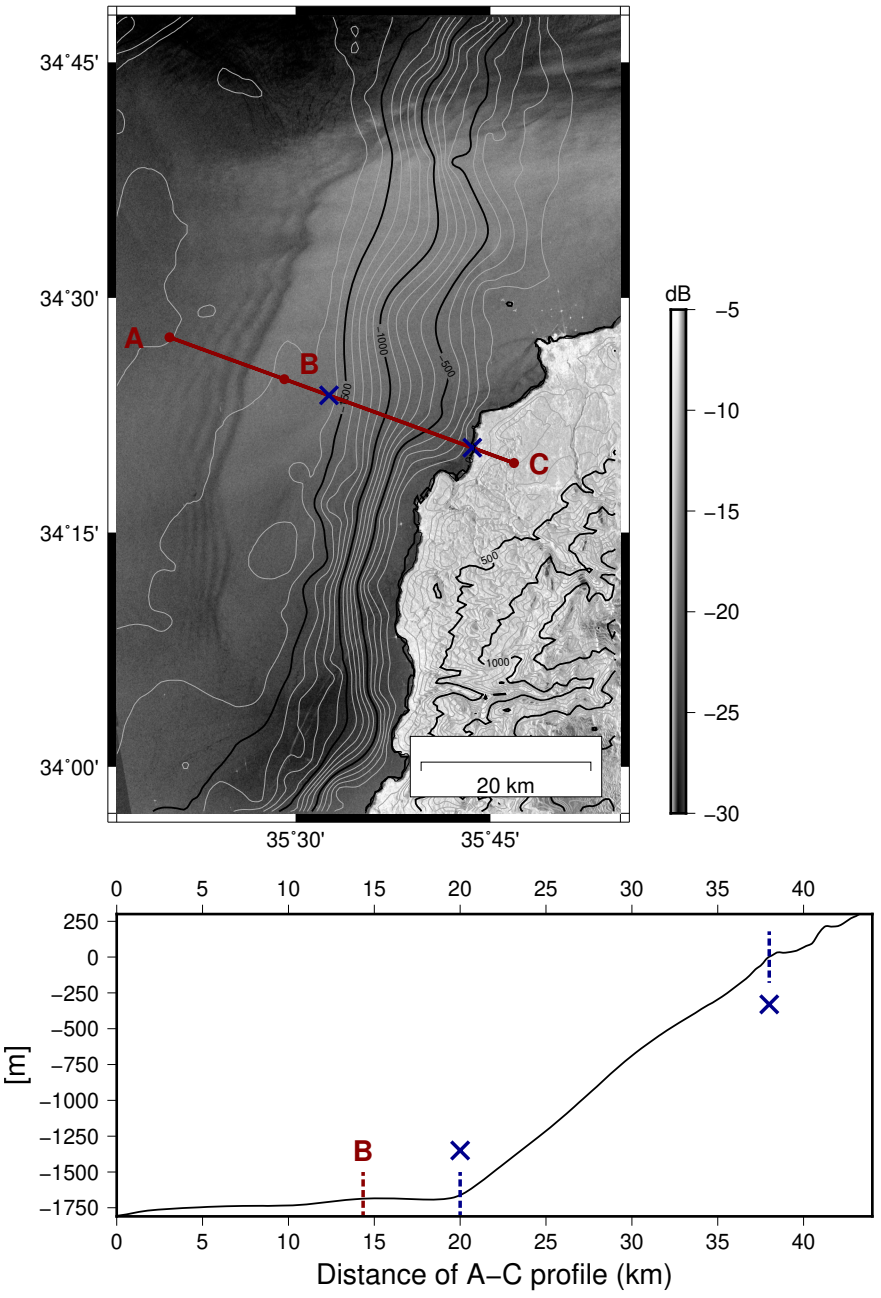

Figure 11. An example of ~~OIWs~~ internal waves in the SAR scene taken at 15:40 on 28 March 2024 near Lebanon, plotted with the contour of bathymetry obtain from ~~GEBOC~~GEBCO (2023). A separate chart illustrates the bathymetry profile along points A and C, sampled every 50 m. The figure contains modified Copernicus Sentinel data [2024].

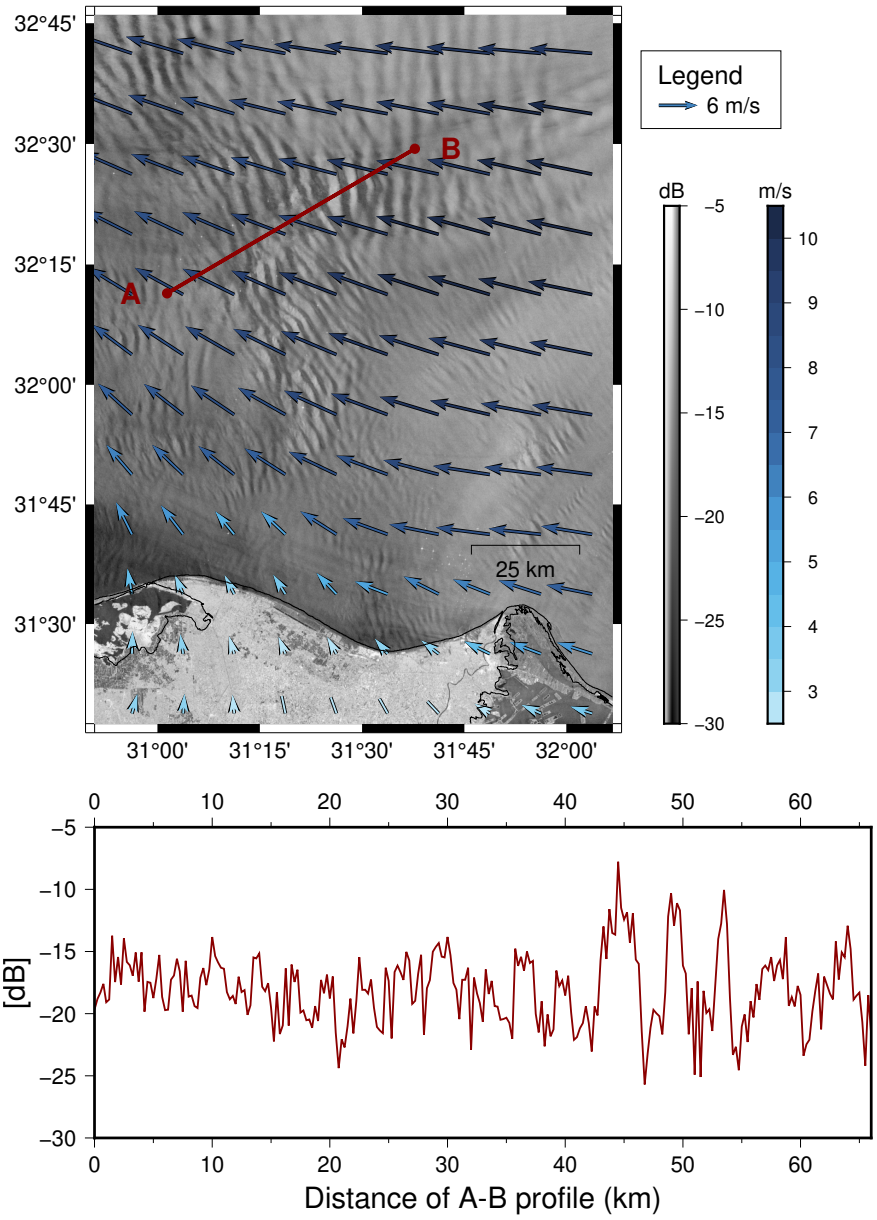

Figure 12. An example of AGWs in the SAR scene taken at 03:51 on 27 May 2023 near Egypt, plotted with the sea surface wind velocity obtain from MDS (CMEMS, c). A separate chart shows the profile of radar backscatter along the red line, sampled every 250 m. The figure contains modified Copernicus Sentinel data [2023]. The coastline was obtained from Wessel and Smith (1996).

turn promotes chlorophyll growth. Mixing can be caused, for example, by the mentioned OIWs, which, like surface waves, can break, leading to mixing. Vertical advection typically occurs due to strong, steady winds, which create a force on the surface layer of the sea, causing it to move in the wind direction. The Coriolis force then deflects this motion to the right in the

northern hemisphere (left in the southern hemisphere), a process called Ekman transport. This results in a 90 shift in the surface layer's movement. This ~~displacement~~ divergence of Ekman transport brings cooler, nutrient-rich water from deeper layers to the surface, known as upwelling, often seen along coastlines where winds blow parallel to the shore (Robinson, 2010; Knauss and Garfield, 2016).

Previous studies have shown areas of enhanced mixing and/or vertical advection in SAR imagery with various causes, such as coastal parallel winds or mixing within cyclonic eddies (Clemente-Colon and Yan, 1999; Alpers and Zeng, 2021). In upwelling regions, low backscatter in SAR imagery can be observed due to increased stability of the ABL (due to reduced wind stress from the lower SST), increased surface water viscosity (which enhances the dampening effect), and the presence of biogenic surface films (see Subsect.4.6) (Clemente-Colon and Yan, 1999). In addition to these mechanisms, the surface divergence and convergence may also play a role (Liu et al., 2016). Previous studies provided a comprehensive explanation of the areas of enhanced mixing or vertical advection in the Mediterranean Sea, for example Bakun and Agostini (2001). In the region of our dataset, the following areas (mostly wind-induced upwelling zones), can be found near the coast: The coastal divergent zone on the south side of Cyprus tends to induce upwelling, especially in summer. On the other hand, the north side of Egypt is dominated by coastal convergence with downwelling, where surface water is brought downward with the flow throughout the year but is most intense in winter. Along the eastern boundary of the Mediterranean Sea, the coasts of Syria, Lebanon, and Israel, the wind generally blows eastward toward the coast. However, the slight right turnings of the wind induce some areas of upwelling.

~~An example of an upwelling area observed by (a) SAR at 03:51 on 19 July 2022 and the supporting materials, (b) SST and (c) chl-*a*, simulated at 00:00 on 19 July 2022 (CMEMS, a; CMEMS, b).~~

Figure 13 (a) shows SAR scenes covering Cyprus at 03:51 on ~~19 July 2022~~ 12 May 2019 and illustrates a possible coastal upwelling area ~~above the red dashed line~~at the southern coast of Cyprus. As suggested in Alpers and Zeng (2021), SST and chl-*a* data can be used to help indicate upwelling areas; Figures 13 (b) and 13 (c) present the corresponding data at 00:00 on ~~19 July 2022~~ 12 May 2019 obtained from the SST MDS (CMEMS, a; Buongiorno Nardelli et al., 2013) and chl-*a* MDS (CMEMS, b; Berthon and Zibordi, 2004; Volpe et al., 2019). ~~The lower SST and higher~~ In most areas, the patterns of both data were similar to each other. However, the southwestern coast of Cyprus had a lower chl-*a* concentration ~~indicate the possible upwellingarea, which~~ than the southeastern coast, though the southwestern and southeastern coasts had similar SST. On the other hand, SAR scenes showed low radar backscatter at both the southwestern and southeastern coasts. Wind speeds were about 2–3 m s^{-3} in the coastal areas according to the hourly sea surface wind velocity from scatterometer and model at 04:00 on 12 May 2019 obtained from MDS (CMEMS, c). Therefore, the low radar backscatter could result from low wind speeds coupled with surface divergence due to upwelling. Additionally, SAR scenes indicate possible surface films that have accumulated as linear features to the west of the dashed red line in the figure. This aligns well with the ~~dark formation shown in the SAR scene~~patterns of SST and chl-*a* concentration.

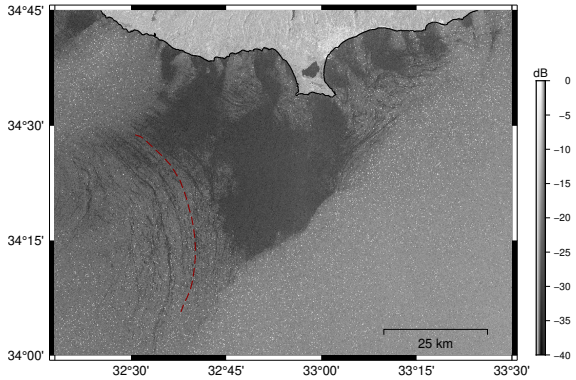

(a) Sentinel-1 SAR

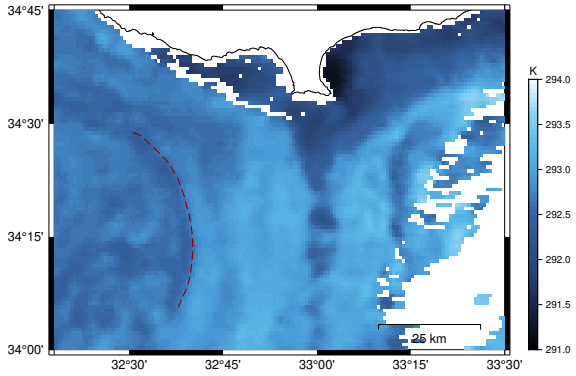

(b) SST

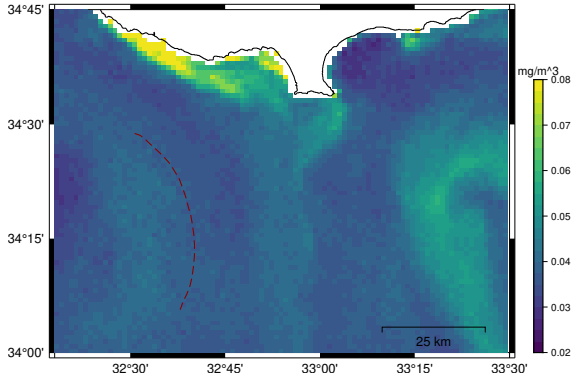

(c) chl-*a*

Figure 13. An example of possible coastal upwelling in southern coast of Cyprus observed by (a) SAR at 03:51 on 12 May 2019 and the supporting materials, (b) SST and (c) chl-*a*, simulated at 00:00 on 12 May 2019 (CMEMS, a; CMEMS, b). The linear features to the left of the red dashed line in SAR indicates the possible surface films accumulations, which aligns well with the patterns of SST and chl-*a*. The figure contains modified Copernicus Sentinel data [2019]. The plotted coastline and borders were obtained from Wessel and Smith (1996).

4.5 Meso- and Submesoscale Eddies

Mesoscale eddies (the prefix "meso" means "intermediate") describe features with radii of about 10 to 200 km and a lifetime of a few days to one year or even longer (Chelton et al., 2007). Submesoscale is defined as slightly smaller than the mesoscale, with horizontal scales of 100 m to 10 km (or less than the first baroclinic mode Rossby radius of deformation (Rd)), vertical scales smaller than the depth of the main pycnocline and a life- time of one day (McWilliams and Molemaker, 2011; Lévy et al., 2012).

Despite a long history in studies of eddy activity, various aspects regarding processes and impacts of meso- and submesoscale eddies still remain unclear. One difficulty in the past and still today is the acquisition of a sufficient database to study these short-lived and small-scale phenomena, especially in ~~in~~ the submesoscale regime. Satellite radar altimeter observes sea surface height (SSH); the difference between SSH and mean sea surface is known as sea surface height anomaly (SSHA), indicating the small displacement of sea surface elevation due to mesoscale eddies. For example, in anticyclonic eddies, the core is less dense (warm core) and has a high SSHA. On the contrary, in cyclonic eddies, the SSHA is lower and the density in the core is higher than in the surrounding area. Chlorophyll, suspended particulates, or other optically reflective materials in the water can reveal the motion in the visible channels (Robinson, 2010). In practice, an altimeter is commonly used for monitoring mesoscale eddies (Alpers et al., 2013), whereas submesoscale eddies are observed with infrared and optical sensors or SAR (Alpers et al., 2014). As the sea surface roughness could be modulated by eddies, SAR can also manifest signatures of eddies on an even smaller scale. Eddies can result in areas of surface convergence and divergence, which under moderate wind conditions appear as bright and dark lines in SAR images (Robinson, 2010). In addition, surface films tend to accumulate along the current shear in eddies. These films can dampen capillary waves and, in this way, enhance SAR signatures of the spiraling shear lines. They are sometimes regarded as "black" eddies in literature; on the other hand, "white" eddies refer to bright curved lines from eddies interacting with waves and current along the shear line at high wind speeds ranged between 7 and ~~12 m s^{-1}~~ 12 m s^{-1} (Karimova and Gade, 2013).

Pegliasco et al. (2021) provided mesoscale eddy detection and tracking methods in the Mediterranean Sea based on products from radar altimeter data from 2000 to 2015 and gave an overview of eddy occurrence in the Mediterranean Sea; the Levantine basin is dominated by anticyclone eddies (warm core rings), which last longer than six months. In the southeastern Levantine basin, SAR observations indicated that the recurrent Cyprus and Shikmona eddies, located south of Cyprus at around 34 N and west and east of 33.5 E, respectively, are dominant (Zodiatis et al., 2005; Gertman et al., 2007; Menna et al., 2012). However, the area is quite complex with cyclonic and anticyclonic eddies interacting with the alongshore cyclonic current and with each other (Gertman et al., 2007; Menna et al., 2012). Figure 14 illustrates such an example of mesoscale eddies forming spiral lines; the SAR scene was taken at 03:52 on 29 September 2022.

4.6 Biogenic Surface Film

There are two types of biogenic surface films that can reduce radar backscatter. Surface active organic molecules with hydrophobic and hydrophilic parts can form a molecular monolayer at the sea surface. The surface waves compress and dilate the molecular

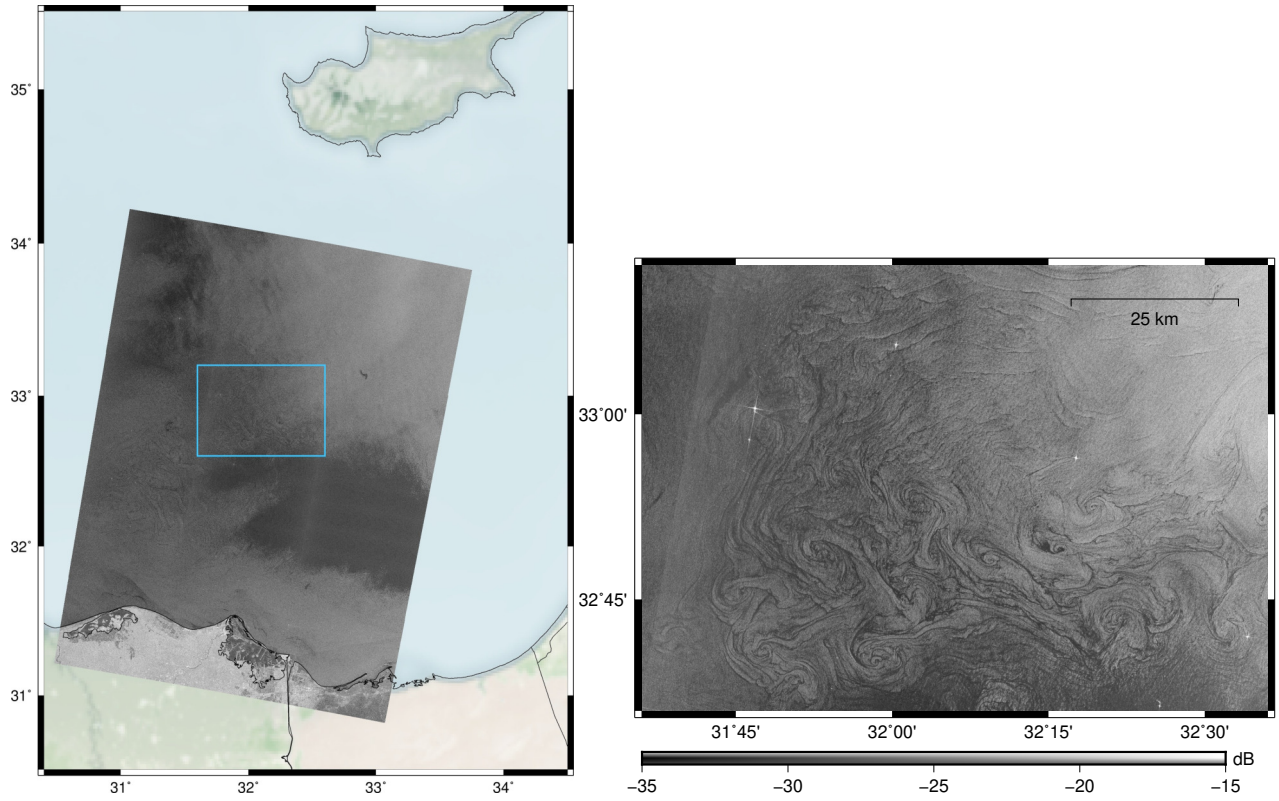

Figure 14. An example of mesoscale eddies observed by SAR at 03:52 on 29 September 2022. The right figure shows the zoomed-in area marked in blue in the left figure. The figure contains modified Copernicus Sentinel data [2022]. The base map of the left figure was obtained from Stevens (2020), and the coastline and borders were obtained from Wessel and Smith (1996).

monolayer, leading to surface tension and surface potential gradients and thus generating the longitudinal Marangoni waves. The interaction of these waves and the transverse gravity capillary waves can result in Marangoni damping and reduce the radar backscattering (**?**Alpers et al., 2017). These surfactants usually originate from the wastewater or remnants of organisms in the water. Another type of biofilm consists of a much thicker layer with a high concentration of viscous floating materials such as phytoplankton, e.g., *Sargassum* and cyanobacteria (Qi et al., 2022). The accumulation of these floating materials decreases the surface tension of the water and dampens the gravity and capillary waves; this effect is similar to the effect of oil discussed in Subsect. 4.1.

Marine phytoplankton are ubiquitous in the sunlit layer of the oceans as they obtain energy through photosynthesis. Satellite-based studies have shown that the Mediterranean Sea generally has low chl-*a* concentration (a useful proxy for phytoplankton biomass), with concentrations often less than $0.2\,\mathrm{mg\ m^{-3}}$ with the exception of some blooming areas in the late winter and early spring (Siokou-Frangou et al., 2010). The overall chl-*a* concentration from satellite and in situ data shows a decline in the trends of west-to-east and north-to-south over the Mediterranean Sea (Siokou-Frangou et al., 2010). Even in blooming seasons,

the chl-*a* concentration was rarely greater than $0.5\,\mathrm{mg\ m^{-3}}$ in the Eastern Mediterranean Sea (Siokou-Frangou et al., 2010), and similar concentrations have been reported from time-series in the Northwestern Mediterranean sea (von Jackowski et al., 2024).

Under a light wind condition, the convergent surface currents accumulate surface films (e.g. algae) along the current shear in fronts and eddies (Gade et al., 2013); these films can dampen the short gravity capillary waves and reduce SAR backscatter. On the other hand, the divergent surface currents make the films less concentrated and the dampening effect is less pronounced (Robinson, 2004). The chl-*a* concentration at the corresponding time and location of Figure 14 had a maximum of $0.059\,\mathrm{mg\ m^{-3}}$ and an average of $0.010\,\mathrm{mg\ m^{-3}}$ (CMEMS, b), which suggests that the spiral patterns of eddies in Figure 14 were not due to accumulations of surface films. It is possible that the patterns were enhanced by a molecular monolayer, but this can not be confirmed without in situ water samples.

4.7 Rain cell

The rain-induced SAR signatures are contributed by a combination of surface scattering, volume scattering and attenuation of radar pulse. Modulations of the sea surface roughness can come from several causes related to the rainfall. The impinging rain drops can either dampen or roughen the sea surface, leading to strong or weak backscattering. In addition, splash products from rain drops can cause scattering. Rain cells usually produce downward airflows (i.e., downdraft), which roughen the sea surface (Alpers et al., 2016). However, splash products from rain drops cause scattering and behind where the rain cell dropped on the sea surface in the direction of wind, the wave is damped (Atlas, 1994). Figure 15 shows such an example of rain cell associated with downdraft, which roughened the sea surface and was shown as bright elliptical area. On top of that, hydrometeors also play important roles in the SAR signatures as they can cause volume scattering and attenuation of the radar pulse, which strengthen and weaken the radar backscattering, respectively. (Danklmayer et al., 2009; Alpers et al., 2016) At C-band, radar signatures for rain are complicated as the decrease or increase of the radar backscatter relative to the background is related to rain rate, wind speed, incidence angle, and time evolution of the rain event (Alpers et al., 2016). For low to moderate high rain rate (smaller than $50\,\mathrm{mm\ hr^{-1}}$), the attenuation is negligible; for heavier rain, the attenuation can be greater than 1 dB (Lin et al., 2001).

Figure 16 (a) shows a SAR scene covering the Israeli coast taken at 03:42 on 24 January 2018. The bright patches, located 5.5 km to 15 km away from the coast and quasi-parallel to it, indicate possible rain-induced signatures. To get an idea of the weather conditions in this region, daily and 10-minute rainfall measurements from the four coastal rain stations were obtained from the Israel Meteorological Service (Ministry of Transport and Road Safety, Israel). The locations of these stations are plotted in Figure 16 (a), and their daily rainfall measurements on 24 January (one day in Israel time, UTC+2) are written in brackets. Though the automated 10-minute rainfall data tend to underestimate the rainfall in major events, they provide an overview of rainfall distribution for the day; Figure 16 (a) illustrates the 10-minute rainfall data from 00:00 to 07:00 on 24 January (UTC). The Hadera Port, Tel Aviv coast, and Ashdod Port stations all reported some rainfall between 02:30 and 05:30. As the rain stations are not directly at the location of rain cells observed from SAR, rainfall at the coasts could be delayed or earlier than rainfall at the water.

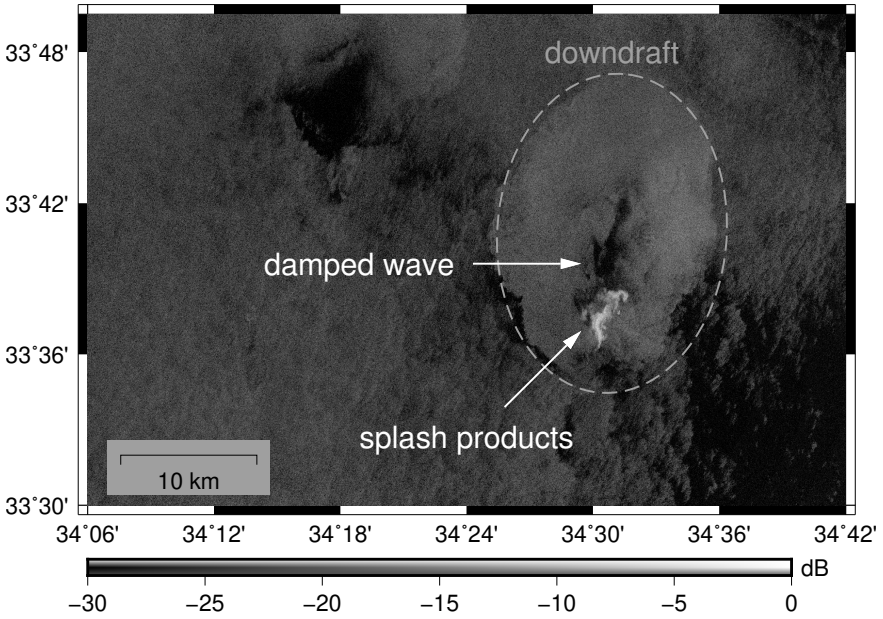

Figure 15. An example of a rain cell with downdraft patterns observed by SAR at 03:43 on 18 October 2022. The figure contains modified Copernicus Sentinel data [2022].

4.8 Others

This section has explained oil slick and a variety of ocean and atmospheric phenomena as origins of SAR signatures. However, wakes and radio frequency interference (RFI), which are related to human activities, also cause remarkable SAR signatures. The following illustrates examples of those signatures, and related literature is provided to help users better understand them.

Moving vessels left tracks in the water as wakes; their structures can be categorized as surface waves (narrow-V wakes and Kelvin wake), turbulent wakes or vortices, and internal waves (Lyden et al., 1988). Although ships can be observed as bright patches in SAR image, ship wake patterns can provide further information such as size, direction, and speed (Rey et al., 1990); therefore, several previous studies focused on detection of ship wakes in SAR images (Lyden et al., 1988; Rey et al., 1990; Shemdin, 1990; Copeland et al., 1995; Graziano et al., 2017; Tings et al., 2023). Figure 17 shows a SAR scene taken at 03:52 on 18 October 2023 near the Port Said off the Egyptian coast. The bright pixels aligned in the south and north directions in the middle of the figure show vessels, along with dark linear features attached to them, which were likely due to wakes. Previous studies also pointed out that wakes from offshore wind turbines could form similar dark formations in SAR images (Christiansen and Hasager, 2005; Li and Lehner, 2013; Ahsbahs et al., 2020); however, they were not commonly seen in this study area.

As SAR is active radar, other radio services (such as communication systems, television networks, surveillance radars for air traffic control, military facilities, meteorological radars, and other spaceborne SAR sensors) with their transmitters on the same or adjacent frequency band to SAR could result in RFI, which usually appear as bright linear signatures in SAR (see

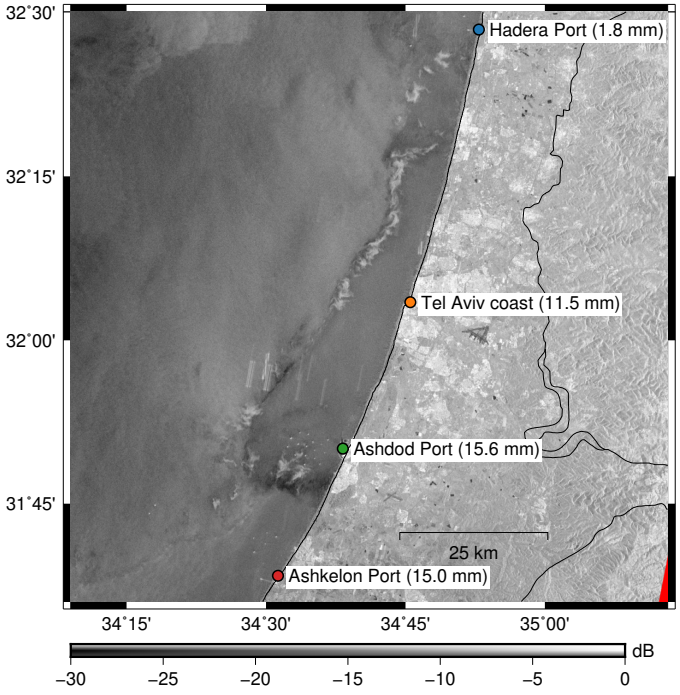

(a) Sentinel-1 SAR, location of rain stations, and the daily rainfall

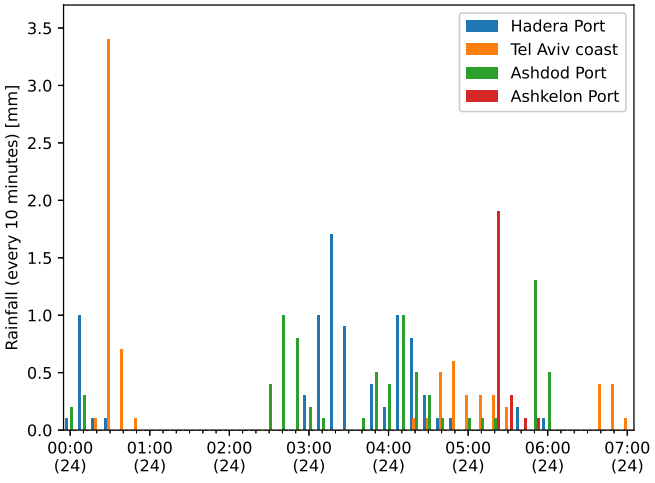

(b) 10-minute rainfall from automated systems

Figure 16. An example of rain cells observed by SAR at 03:42 on 24 January 2018, along with (a) daily and (b) 10-minute rainfall data obtained from the Israel Meteorological Service (Ministry of Transport and Road Safety, Israel). Figure (a) contains modified Copernicus Sentinel data [2018]. The coastline and borders were obtained from Wessel and Smith (1996).

Figure 18). Several previous studies discussed the influence of those RFI on different frequency bands and proposed removal

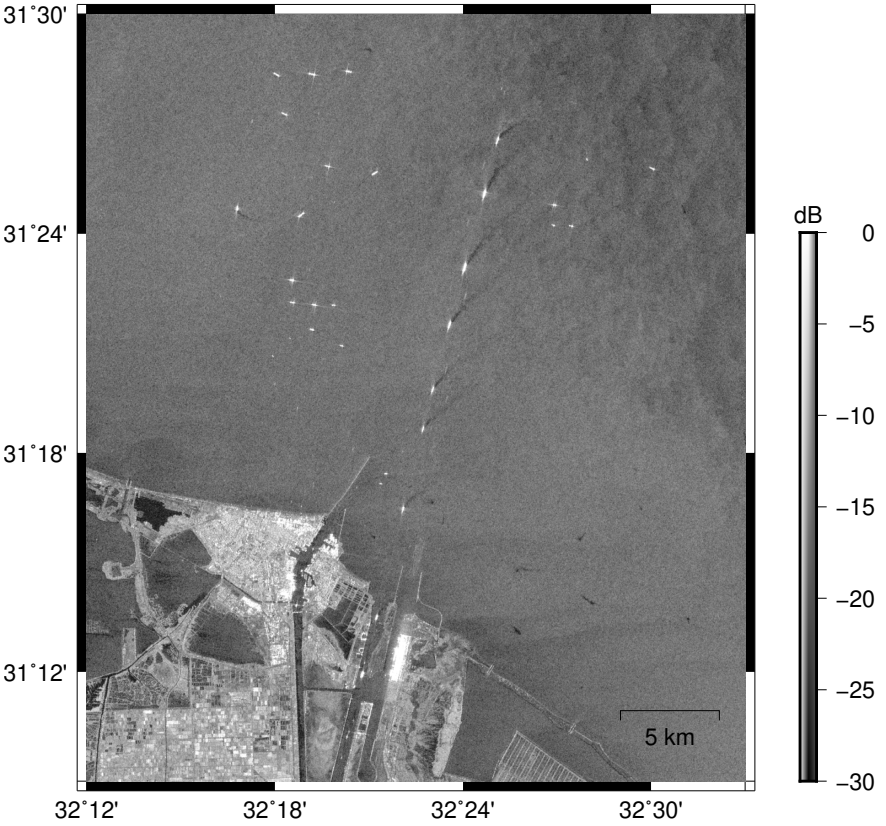

Figure 17. An example of ship wakes observed in a SAR scene taken at 03:52 on 18 October 2023 near the Port Said. The figure contains modified Copernicus Sentinel data [2023].

methods (Miller et al., 1997; Rosen et al., 2008; Meyer et al., 2013; Natsuaki et al., 2017; Monti-Guarnieri et al., 2017; Franceschi et al., 2021). Thanks to researchers working on the detecting and identifying RFI in Sentinel-1 data, the operational RFI detection and mitigation was activated in the SAR processor on 23 March 2022 (Franceschi et al., 2022; Hajduch et al., 2022). In other words, since then, Sentinel-1 Level-1 data has been produced under consideration of RFI mitigation. However, readers should keep the effect of RFI in mind as they might still find some data with certain RFI not being mitigated; such examples are shown in Figure 19.

4.9 Example List

This subsection lists all Sentinel-1 SAR scenes used in the examples provided in this section. Some of the signatures covered a larger area than how they are shown in the paper; however, if readers wish to see the original SAR scenes, the information provided in Table 3 should be enough for obtaining them from the Copernicus Data Space Ecosystem. In addition, the

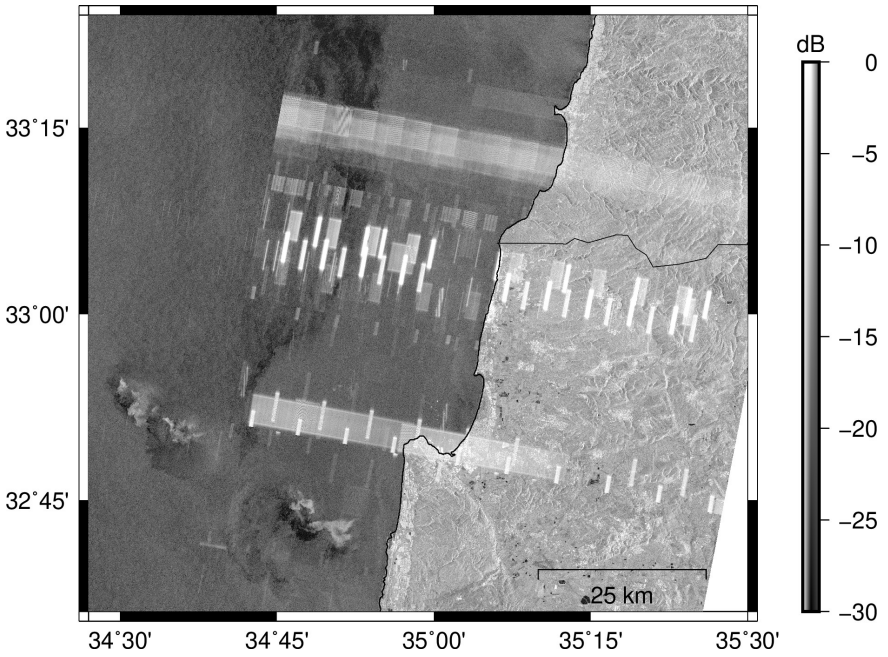

Figure 18. An example of RFI observed in a SAR scene taken at 03:43 on 21 October 2018, along with some rain cell signatures. The figure contains modified Copernicus Sentinel data [2018]. The plotted coastline and borders were obtained from Wessel and Smith (1996).

corresponding supplementary materials used in the explanations are also listed; however, users should not limit themselves to the selection of supplementary data.

5 Usage Notes

5.1 Performance Evaluation

To make it possible for users who wish to compare their model performance with other studies, the performance of a custom-trained object detector from a previous study (Yang et al., 2024) was evaluated and is shown in this subsection. The performance on image patches with and without oil objects (i.e. *oil set* and *no-oil set*) are evaluated separately. In the following, the annotations from this published dataset are regarded as ground truth and abbreviated to *gt*. However, it shall be noted that even though the authors who prepared the dataset tried to avoid human errors, these annotations might still include false annotations. Note that this data descriptor is not intended to have a comprehensive discussion on the performance; therefore, this subsection only shows the measures, but readers can refer to Yang et al. (2024) for interpretation of the results.

For performance evaluation of object detection algorithms, intersection over union (IoU) is commonly used to indicate how accurate the detection (or known as prediction, which is a common term used in the object detection field) is compared to the

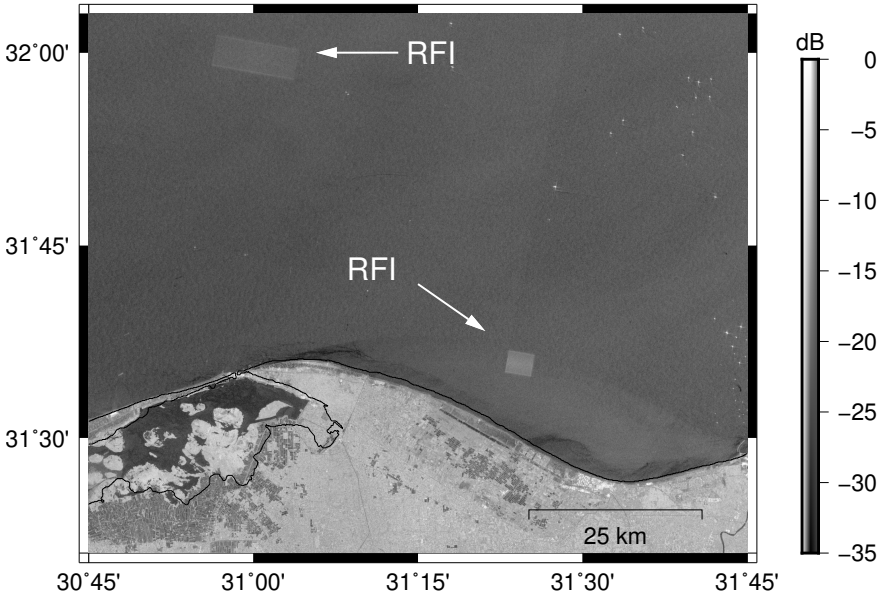

Figure 19. An example of RFI observed in a SAR scene taken at 03:52 on 24 September 2023; the RFI was not detected and mitigated by the SAR processor. The figure contains modified Copernicus Sentinel data [2023]. The plotted coastline were obtained from Wessel and Smith (1996).

ground truth and is defined as (Everingham et al., 2010):

$$IoU = \frac{\text{area}(B_{detn} \cap B_{gt})}{\text{area}(B_{detn} \cup B_{gt})}, \tag{3}$$

where ~~$B_p \cap B_g$ and $B_p \cup B_g$~~ $B_{detn} \cap B_{gt}$ and $B_{detn} \cup B_{gt}$ refer to the intersection and union of the bounding boxes of the ~~prediction (B_p~~detection (B_{detn}) and the ground truth (~~B_g~~B_{gt}), respectively.

Based on IoU, the detections can be categorized as true positives (TP) or false positives (FP). TP shows the detections intersecting with the ground truth and with their IoU greater than a given threshold. On the other hand, FP shows the detections with no intersection with the ground truth, or their IoU values are smaller than the threshold. If we change the perspective and focus on ground truths, TP and false negatives (FN) are used, showing the ground truths with and without corresponding detections, respectively. The definition of one oil object might differ between ground truths and detections for some complicated cases, resulting in more than one detection referring to one ground truth. Therefore, the numbers of TP for detections and ground truths might differ; in the following, they are referred to as ~~TP (detn) and TP (gt)~~TP_{detn} and TP_{gt}, respectively. To easily focus on the negative results of the models, the false discovery rate (FDR) and false negative rate (FNR) are provided, they are defined as follows:

$$FDR = \frac{FP}{TP_{detn} + FP},$$
$$FNR = \frac{FN}{TP_{gt} + FN}. \tag{4}$$

Table 3. List of Copernicus Sentinel-1 scenes used as examples provided in Sect. 4, along with their corresponding supplementary data.

Fig.	Signature	Start Date & Time (YYYY-MM-DD hh:mm:ss)		Abs. orbit	Mission ID	Product ID	Supplementary Data
7 (a)	Oil slick	2022-11-03	15:49:28	045732	057835	D069	
7 (b)	Oil slick	2022-11-04	03:52:42	045739	057870	6C96	
8	Wind	2023-08-02	03:44:34	049691	05F9AE	7321	• Sea surface wind velocity (CMEMS, c)
			03:44:59			D5EB	
9 (a)	Wind	2022-09-24	03:43:41	045141	056512	74D8	• Sea surface wind velocity (CMEMS, c)
			03:44:06			F1AB	• Bathymetry and terrain chart (GEBCO, 2023)
10	Wind	2023-01-27	03:52:39	046964	05A1FB	3A5D	• Sea surface wind velocity (CMEMS, c)
11	Internal waves	2024-03-28	15:41:26	053184	0671A3	05B8	• Bathymetry and terrain chart (GEBCO, 2023)
			15:41:51			B6E5	
12	AGWs	2023-05-27	03:52:16	048714	05D8D7	EF08	• Sea surface wind velocity (CMEMS, c)
			03:52:41			2FEB	
13	Upwelling	2019-05-12	03:51:18	027189	0310AB	EEF7	• SST (CMEMS, a)
			03:51:43			00AD	• chl-*a* concentration (CMEMS, b)
							• Sea surface wind velocity (CMEMS, c)
14	Eddies	2022-09-29	03:52:17	045214	056776	5889	
			03:52:42			04BC	
15	Rain cell	2022-10-18	03:43:42	045491	057070	3FB9	
			03:44:07			DC74	
16	Rain cell	2018-01-24	03:43:41	020291	022A5B	C066	• Rainfall observation
			03:44:06			A779	(Ministry of Transport and Road Safety, Israel)
17	Wakes	2023-10-18	03:52:47	050814	061FD2	6D11	
18	RFI	2018-10-21	03:43:02	013245	0187C4	ABBF	
19	RFI	2023-09-24	03:52:47	050464	0613CC	CF0D	

Table 4 shows the performance of the two ~~models~~ object detectors applied to a near real-time automated oil spill detection and early warning system ~~that~~ as *YODA-enh* and *YODA-enh-aug1*, which were claimed to perform well in a previous study (Yang et al., 2024). Thresholds for filtering out the objects which have low confidence scores and IoU were applied. Note that due to different image patches used in the performance evaluation and a slightly different way of calculation, these numbers differ from those shown in the paper.

Regarding the performance on the *no-oil set*, as there are no objects inside, the measures for object detection algorithms are not appropriate. Here, image patches are simply marked as two categories, one with no detections inside and another with one or more detections inside. The former shows that the detector performs well and is not confused by the look-alikes. The latter

Table 4. Performance evaluation of the models from a previous study (Yang et al., 2024) on the *oil set*.

Model		Subset	# img	# gt	# detn	# TP		# FP	# FN	FDR[%]	FNR[%]
						(gt)	(detn)				
YODA-enh	(a)	ow	990	2284	1029	1154	1023	6	1249	0.58	51.98
		oc	392	941	344	353	296	48	623	13.95	63.83
	(b)	ow	990	2284	468	515	468	0	1782	0.00	77.58
		oc	392	941	137	148	130	7	798	5.11	84.36
	(c)	ow	990	2284	468	426	425	43	1858	9.19	81.35
		oc	392	941	137	125	125	12	816	8.76	86.72
YODA-enh-aug1	(a)	ow	990	2284	787	1487	787	0	877	0.00	37.10
		oc	392	941	147	296	146	1	655	0.68	68.87
	(b)	ow	990	2284	318	520	318	0	1765	0.00	77.24
		oc	392	941	55	101	55	0	842	0.00	89.29
	(c)	ow	990	2284	318	42	42	276	2242	86.79	98.16
		oc	392	941	55	18	18	37	923	67.27	98.09

(a) $thres_{\text{score}} = 0.0$, $thres_{\text{IoU}} = 0.0$; (b) $thres_{\text{score}} = 0.5$, $thres_{\text{IoU}} = 0.0$; (c) $thres_{\text{score}} = 0.5$, $thres_{\text{IoU}} = 0.5$

indicates that the detector can be confused with specific signatures inside the image patches. Figure 20 shows the results of the two models on the *no-oil set* with different confidence score thresholds.

5.2 Technical Notes

There are some additional technical notes for the users:

- The annotation of the objects follows the Pascal VOC XML format; users who have their labels in different annotation format, should carefully convert the labels into the format they used. ~~A Python 3 function for converting from XML format to YOLO format is provided as a reference in Appendix **??**.~~
- The published dataset has only one class (i.e. oil) objects; if users have different definitions of classes in their work, they would have to make sure the performance evaluation is still valid.
- For training an object detector, the authors would suggest using a dataset without masking out the land area as some coastal information might be helpful for the detectors to learn as background information. If users wish to apply land masks to the published dataset, they can generate the corresponding mask out scenes by loading the geoinformation provided along with the dataset. A program for land masking is also provided in the GitHub repository associated with this paper.

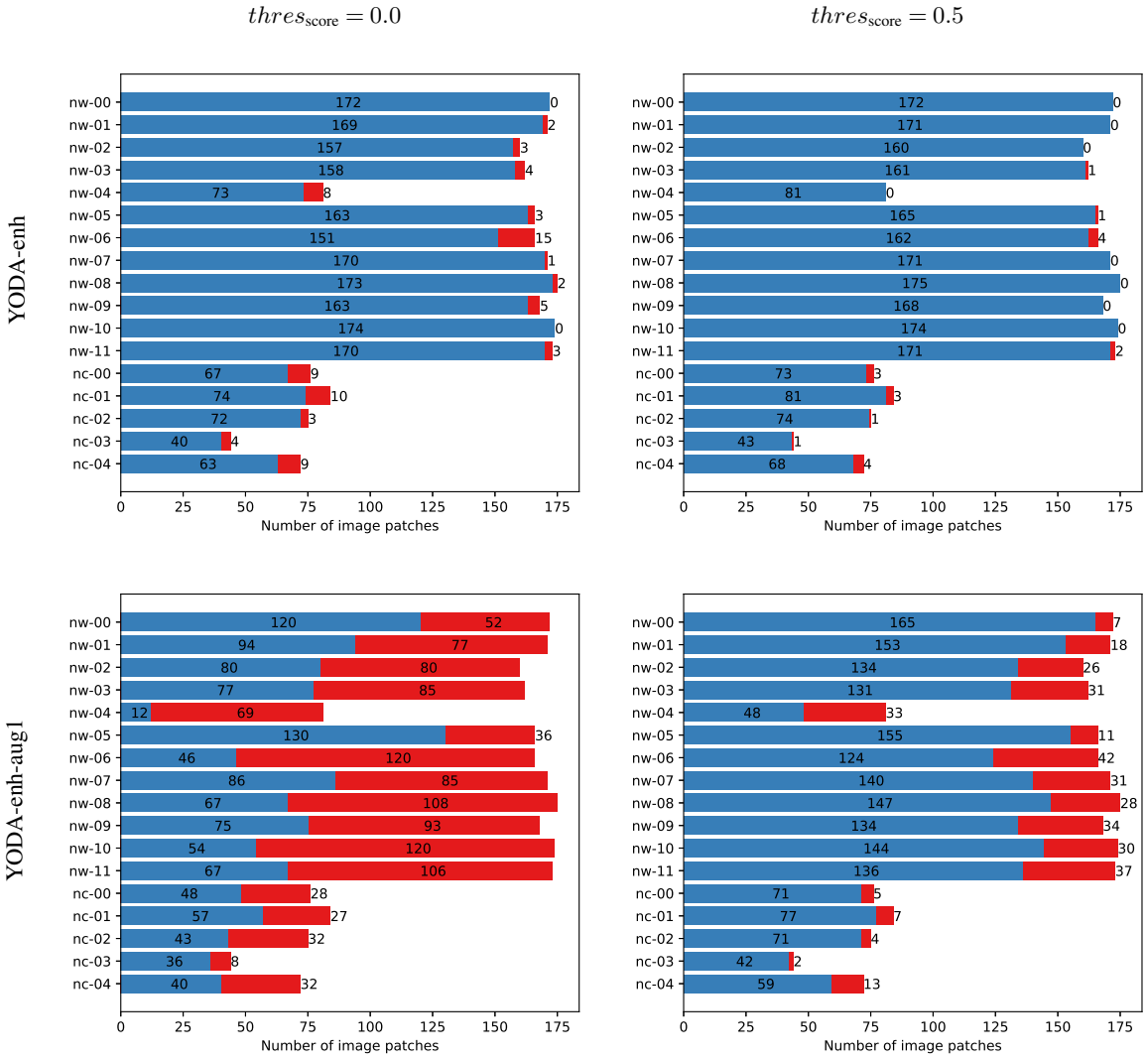

Figure 20. Numbers of image patches in the *no-oil set* that the models return detections (in red) and without any detection (in blue).

- For an operational oil slick detection system, land masks should be considered as they can help improve the efficiency of the system and avoid false positives in the land areas. Global land masks can be obtained from sources such as Wessel and Smith (1996) and Karin (2020).

- For studies focusing on different study areas, the sources of oil slicks and geographic settings might be different from the dataset and, therefore, result in poor performance. However, it could help understand how one local model performs in a different area and lead to further discussion.

- Even though the authors aim to provide a published dataset as a test set for comparing models with different studies, users can also use the dataset to (further) train their algorithms.

- Users are encouraged to check the dataset themselves and adjust the labels when they do not fit the "style" of annotations from the users. ~~Python 3 functions for plotting image patches along with their annotations into JPG are provided as references in Appendix ??.~~

6 Summary

This data descriptor presents a dataset containing oil slicks, look-alikes, and other notable ocean phenomena, collected for the purpose of SAR image analysis. It provides explanations and examples of various ocean SAR signatures, supported by supplementary materials, to help users better understand the sources of these signatures.

The descriptor also includes a performance evaluation of a model from a previous study (Yang et al., 2024), which was tested on this dataset. This allows users who have trained their own oil spill detectors to compare their model performance with other studies. Additionally, the dataset is a valuable resource for newcomers to the oil slick detection community, providing a ready-made dataset for starting their work.

Recent research in SAR oil spill detection has increasingly focused on machine learning techniques. Given the diverse backgrounds of researchers in this fieldÔÇöranging from remote sensing and machine learning to oceanographyÔÇöthis data descriptor aims to bridge the knowledge gap for those less familiar with oceanographic concepts. Readers are encouraged to consult specialized textbooks on SAR signal processing (Woodhouse, 2006), physical oceanography (Knauss and Garfield, 2016), and SAR oceanography (Robinson, 1983, 2004, 2010) for more comprehensive explanations.

7

The dataset with oil slicks, look-alikes, and other remarkable phenomena covering the Eastern Mediterranean Sea in 2019 can be accessed through PANGAEA via https://doi.pangaea.de/10.1594/PANGAEA.980773 (Yang and Singha, 2025). The image patches are normalized to 0–255 and saved in an 8-bit JPG format. The oil annotations are in Pascal VOC XML format. A data table recording the Sentinel-1 ID of all the image patches inside the dataset is also provided; therefore, the original Sentinel-1 products can be downloaded via the Copernicus Data Space Ecosystem. The code related to working

with the dataset, including the evaluation of performacne, is available on a public github repository under https://github.com/yi-jie-yang/dataset_DARTIS_2019 (last access: 21 November 2025).

Appendix A: Python code

This appendix provides some Python 3 functions to help users quickly get along with the dataset. A function for converting Pascal VOC XML format into YOLO format is provided as follows:

```
def xml2yolo(img_width, img_height, bbox):
    xmin, xmax, ymin, ymax = bbox
    dw = 1.0/img_width
    dh = 1.0/img_height
    x_center = ((xmin+xmax)/2.0)*dw
    y_center = ((ymin+ymax)/2.0)*dh
    w = (xmax-xmin)*dw
    h = (ymax-ymin)*dh
    return [x_center, y_center, w, h]
```

Functions for plotting image patch along with its annotations into a JPG image:

```
import xml.etree.ElementTree as ET
from PIL import Image, ImageDraw

def load_xml(xml):
    tree = ET.parse(xml)
    root = tree.getroot()

    # Save object positions
    list_bbox = []
    for obj in root.findall("object"):
        bbox = obj.find("bndbox")
        list_bbox.append([
            int(bbox.find("xmin").text),
            int(bbox.find("ymin").text),
            int(bbox.find("xmax").text),
            int(bbox.find("ymax").text)
        ])
    return list_bbox

def plot_patch_label(img_file, img_out, xml):
```

```
    # Load annotations and image patch
    list_bbox = load_xml(xml)
    img = Image.open(img_file)
690 -
    # Plot annotations
    img_ann = ImageDraw.Draw(img)
    for bbox in list_bbox:
        img_ann.rectangle(bbox,
695         fill=None, outline=255,
            width=2)
-
    # Resize image
    w, h = img.size
700 if w > 640 or h > 640:
        img = img.resize(
            (640,640), Image.LANCZOS)
--
    # Save image
705 img.save(img_out)
```

Appendix A: Data Table

Subsect. 2.2 provides explanations on how the dataset is organized and how their information is stored in the data table. To explain better and provide information about the image patches shown in this article, the data information of those image
710 patches is extracted and displayed in the following tables; the original data table can be found in the published dataset. Tables A1 and A3 show the patch names, patch dimensions, and corner coordinates of the patches in the WGS84 geocentric coordinate system. Tables A2 and A4 are continuous from Tables A1 and A3, respectively, showing the product start and stop date time and the product ID. Table A5 contains the object information, including corner coordinates of the objects in the WGS84 geocentric coordinate system, object positions referring to the corresponding image patches along the range and
715 azimuth direction, and the bounding box size in pixels. Tables A1 and A3 record the information of image patches from *no-oil set*, which are mentioned in Figures 2 and 6. On the other hand, Tables A3, A4, and A5 indicate the information of image patches from *oil set*, which are mentioned in Figure 5.

Table A1.

tag	patch_name	patch_ width	height	ul_lon	ul_lat	ur_lon	ur_lat	br_lon	br_lat	bl_lon	bl_lat
nw-0547-03-000044	S1_20190319_035039_035218_VV_95	640	640	31.1062	33.3788	30.9706	33.3977	30.9475	33.2826	31.0829	33.2636
nw-0553-03-000050	S1_20190412_035040_035219_VV_12	640	640	32.3278	35.3925	32.1889	35.4121	32.1639	35.2971	32.3025	35.2774
nw-0603-03-000100	S1_20190803_035856_040035_VV_14	640	640	30.0576	35.9321	29.9176	35.9513	29.8933	35.8362	30.0331	35.8169
nw-0609-03-000106	S1_20190827_035858_040037_VV_21	640	640	29.9765	35.5871	29.8371	35.6063	29.8131	35.4911	29.9522	35.4719
nw-0165-00-000165	S1_20191220_035048_035227_VV_101	640	640	31.8779	34.4780	31.7405	34.4975	31.7165	34.3823	31.8537	34.3628
nw-0307-01-000135	S1_20191102_154017_154157_VV_101	640	640	33.9115	33.7039	34.0472	33.7251	34.0212	33.8404	33.8853	33.8192
nw-0446-02-000103	S1_20190711_035121_035303_VV_33	640	640	32.7978	35.3136	32.6592	35.3338	32.6336	35.2186	32.7720	35.1984
nw-0651-03-000148	S1_20191214_035125_035306_VV_294	640	640	31.8042	35.2799	31.6654	35.2990	31.6412	35.1839	31.7798	35.1648
nw-0687-04-000022	S1_20190406_035117_035258_VV_81	640	640	31.6319	34.9168	31.4937	34.9359	31.4704	34.8207	31.6084	34.8017
nw-0763-05-000017	S1_20190207_033454_033634_VV_22	640	640	35.6396	34.5452	35.5020	34.5642	35.4777	34.4492	35.6150	34.4302
nw-0997-06-000085	S1_20190522_155643_155737_VV_5	640	640	31.7808	32.6882	31.9154	32.7076	31.8919	32.8231	31.7572	32.8037
nw-1203-07-000125	S1_20190927_154017_154157_VV_86	640	640	34.0069	35.1136	34.1451	35.1343	34.1199	35.2495	33.9815	35.2289
nw-1331-08-000082	S1_20190531_034300_034440_VV_41	640	640	35.0884	35.5409	34.9495	35.5613	34.9242	35.4460	35.0630	35.4256
nw-1523-09-000099	S1_20190604_154838_155018_VV_33	640	640	32.7407	34.1620	32.8774	34.1821	32.8526	34.2972	32.7157	34.2772
nw-1679-10-000087	S1_20190821_035934_040114_VV_69	640	640	30.5790	31.6785	30.4463	31.6996	30.4210	31.5842	30.5535	31.5631
nw-1883-11-000117	S1_20190612_034300_034440_VV_90	640	640	35.2993	34.5986	35.1620	34.6195	35.1359	34.5043	35.2729	34.4834
nc-0009-00-000009	S1_20190216_035850_040029_VV_87	640	640	30.8020	31.5517	30.6695	31.5730	30.6439	31.4577	30.7763	31.4364
nc-0140-01-000064	S1_20191028_034227_034407_VV_119	640	640	35.5257	33.8044	35.3898	33.8258	35.3633	33.7105	35.4990	33.6891
nc-0207-02-000047	S1_20190927_035049_035228_VV_9	640	640	33.5185	34.7990	33.3810	34.8201	33.3556	34.7048	33.4929	34.6836
nc-0253-03-000018	S1_20190529_154748_154928_VV_50	640	640	32.2326	34.9748	32.3706	34.9952	32.3451	35.1106	32.2069	35.0903
nc-0325-04-000046	S1_20190909_035125_035306_VV_38	640	640	33.9199	34.9777	33.7821	34.9992	33.7550	34.8839	33.8925	34.8624

Table A2.

tag	start_time	end_time	Sentinel_ID
nw-0547-03-000044	2019-03-19T03:50:39	2019-03-19T03:52:18	S1B_IW_GRDH_1SDV_20190319T035104_20190319T035129_015418_01CDFB_86C8.SAFE
nw-0553-03-000050	2019-04-12T03:50:40	2019-04-12T03:52:19	S1B_IW_GRDH_1SDV_20190412T035040_20190412T035105_015768_01D985_9F88.SAFE
nw-0603-03-000100	2019-08-03T03:58:56	2019-08-03T04:00:35	S1B_IW_GRDH_1SDV_20190803T035856_20190803T035921_017416_020C16_EF88.SAFE
nw-0609-03-000106	2019-08-27T03:58:58	2019-08-27T04:00:37	S1B_IW_GRDH_1SDV_20190827T035858_20190827T035923_017766_0216ED_C8C4.SAFE
nw-0165-00-000165	2019-12-20T03:50:48	2019-12-20T03:52:27	S1B_IW_GRDH_1SDV_20191220T035048_20191220T035113_019443_024BA5_28B4.SAFE
nw-0307-01-000135	2019-11-02T15:40:17	2019-11-02T15:41:57	S1A_IW_GRDH_1SDV_20191102T154107_20191102T154132_029734_036369_FE5F.SAFE
nw-0446-02-000103	2019-07-11T03:51:21	2019-07-11T03:53:03	S1A_IW_GRDH_1SDV_20190711T035121_20190711T035146_028064_032B5E_8132.SAFE
nw-0651-03-000148	2019-12-14T03:51:25	2019-12-14T03:53:06	S1A_IW_GRDH_1SDV_20191214T035125_20191214T035150_030339_037875_3C8E.SAFE
nw-0687-04-000022	2019-04-06T03:51:17	2019-04-06T03:52:58	S1A_IW_GRDH_1SDV_20190406T035117_20190406T035142_026664_02FE02_C5A5.SAFE
nw-0763-05-000017	2019-02-07T03:34:54	2019-02-07T03:36:34	S1A_IW_GRDH_1SDV_20190207T033454_20190207T033519_025818_02DF3B_8839.SAFE
nw-0997-06-000085	2019-05-22T15:56:43	2019-05-22T15:57:37	S1B_IW_GRDH_1SDV_20190522T155643_20190522T155712_016359_01ECA7_4C33.SAFE
nw-1203-07-000125	2019-09-27T15:40:17	2019-09-27T15:41:57	S1A_IW_GRDH_1SDV_20190927T154132_20190927T154157_029209_035141_93D0.SAFE
nw-1331-08-000082	2019-05-31T03:43:00	2019-05-31T03:44:40	S1A_IW_GRDH_1SDV_20190531T034300_20190531T034325_027466_031954_5014.SAFE
nw-1523-09-000099	2019-06-04T15:48:38	2019-06-04T15:50:18	S1A_IW_GRDH_1SDV_20190604T154928_20190604T154953_027532_031B5A_1FA3.SAFE
nw-1679-10-000087	2019-08-21T03:59:34	2019-08-21T04:01:14	S1A_IW_GRDH_1SDV_20190821T040049_20190821T040114_028662_033E63_B88E.SAFE; S1A_IW_GRDH_1SDV_20190821T040024_20190821T040049_028662_033E63_3BDB.SAFE
nw-1883-11-000117	2019-06-12T03:43:00	2019-06-12T03:44:40	S1A_IW_GRDH_1SDV_20190612T034325_20190612T034350_027641_031EA9_55D4.SAFE
nc-0009-00-000009	2019-02-16T03:58:50	2019-02-16T04:00:29	S1B_IW_GRDH_1SDV_20190216T035940_20190216T040005_014966_01BF36_8C52.SAFE
nc-0140-01-000064	2019-10-28T03:42:27	2019-10-28T03:44:07	S1B_IW_GRDH_1SDV_20191028T034252_20191028T034317_018670_0232F7_237B.SAFE
nc-0207-02-000047	2019-09-27T03:50:49	2019-09-27T03:52:28	S1B_IW_GRDH_1SDV_20190927T035049_20190927T035114_018218_0224DC_62D9.SAFE
nc-0253-03-000018	2019-05-29T15:47:48	2019-05-29T15:49:28	S1B_IW_GRDH_1SDV_20190529T154903_20190529T154928_016461_01EFC4_CD23.SAFE
nc-0325-04-000046	2019-09-09T03:51:25	2019-09-09T03:53:06	S1A_IW_GRDH_1SDV_20190909T035125_20190909T035150_028939_034806_F874.SAFE

Table A3.

tag	patch_name	patch_ width	height	ul_lon	ul_lat	ur_lon	ur_lat	br_lon	br_lat	bl_lon	bl_lat
ow-0267-01-000666 ow-0267-02-000667 ow-0267-03-000668	S1_20190512_035118_035259_VV_1	640	640	31.4543	32.2251	31.3205	32.2448	31.2968	32.1295	31.4305	32.1099
ow-0276-01-000680 ow-0276-02-000681	S1_20190515_160406_160546_VV_0	640	640	30.0586	31.4844	30.1915	31.5039	30.1681	31.6190	30.0351	31.5996
ow-0438-01-001124 ow-0438-02-001125 ow-0438-03-001126 ow-0438-04-001127 ow-0438-05-001128	S1_20190622_035930_040110_VV_0	1294	1294	31.5372	33.7382	31.2640	33.7815	31.2107	33.5484	31.4840	33.5051
ow-0447-01-001152 ow-0447-02-001153 ow-0447-03-001154 ow-0447-04-001155 ow-0447-05-001156	S1_20190623_035044_035223_VV_0	977	977	32.8049	31.9612	32.6023	31.9935	32.5633	31.8176	32.7660	31.7852
ow-0463-01-001189 ow-0463-02-001190	S1_20190624_034301_034441_VV_0	1748	1748	33.5068	32.5655	33.1398	32.6186	33.0742	32.3041	33.4412	32.2509
ow-0643-01-001540 ow-0643-02-001541 ow-0643-03-001542 ow-0643-04-001543 ow-0643-05-001544 ow-0643-06-001545 ow-0643-07-001546 ow-0643-08-001547 ow-0643-09-001548 ow-0643-10-001549	S1_20190821_154753_154933_VV_12	640	640	32.8779	31.8404	33.0111	31.8609	32.9864	31.9765	32.8532	31.9560

Table A4.

tag	start_time	end_time	Sentinel_ID
ow-0267-01-000666	2019-05-12T03:51:18	2019-05-12T03:52:59	S1A_IW_GRDH_1SDV_20190512T035208_20190512T035233_027189_0310AB_E893.SAFE
ow-0267-02-000667			
ow-0267-03-000668			
ow-0276-01-000680	2019-05-15T16:04:06	2019-05-15T16:05:46	S1B_IW_GRDH_1SDV_20190515T160431_20190515T160456_016257_01E988_22CD.SAFE
ow-0276-02-000681			
ow-0438-01-001124	2019-06-22T03:59:30	2019-06-22T04:01:10	S1A_IW_GRDH_1SDV_20190622T035955_20190622T040020_027787_0322FB_5391.SAFE
ow-0438-02-001125			
ow-0438-03-001126			
ow-0438-04-001127			
ow-0438-05-001128			
ow-0447-01-001152	2019-06-23T03:50:44	2019-06-23T03:52:23	S1B_IW_GRDH_1SDV_20190623T035134_20190623T035159_016818_01FA62_D8E1.SAFE
ow-0447-02-001153			
ow-0447-03-001154			
ow-0447-04-001155			
ow-0447-05-001156			
ow-0463-01-001189	2019-06-24T03:43:01	2019-06-24T03:44:41	S1A_IW_GRDH_1SDV_20190624T034351_20190624T034416_027816_0323DB_253E.SAFE
ow-0463-02-001190			
ow-0643-01-001540	2019-08-21T15:47:53	2019-08-21T15:49:33	S1B_IW_GRDH_1SDV_20190821T154818_20190821T154843_017686_021461_4D57.SAFE
ow-0643-02-001541			
ow-0643-03-001542			
ow-0643-04-001543			
ow-0643-05-001544			
ow-0643-06-001545			
ow-0643-07-001546			
ow-0643-08-001547			
ow-0643-09-001548			
ow-0643-10-001549			

Table A5.

tag	obj_								obj_patchloc_				label_size
	ul_lon	ul_lat	ur_lon	ur_lat	br_lon	br_lat	bl_lon	bl_lat	xmin	ymin	xmax	ymax	
ow-0267-01-000666	31.3541	321779	31.3458	32.1791	31.3445	32.1728	31.3528	32.1716	420	334	460	369	1400
ow-0267-02-000667	31.3592	322254	31.3475	32.2271	31.3427	32.2038	31.3544	32.2021	442	74	498	203	7224
ow-0267-03-000668	31.4055	321367	31.3875	32.1394	31.3855	32.1297	31.4035	32.1270	142	515	228	569	4644
ow-0276-01-000680	30.1084	315432	30.1230	31.5454	30.1197	31.5616	30.1051	31.5594	289	278	359	368	6300
ow-0276-02-000681	30.1124	315529	30.1315	31.5557	30.1262	31.5820	30.1071	31.5792	317	327	409	473	13432
ow-0438-01-001124	31.4387	336672	31.4193	33.6703	31.4186	33.6674	31.4381	33.6643	376	464	468	480	1472
ow-0438-02-001125	31.4521	336606	31.4299	33.6641	31.4287	33.6589	31.4509	33.6554	308	488	413	517	3045
ow-0438-03-001126	31.5102	336209	31.4874	33.6246	31.4856	33.6168	31.5085	33.6132	1	651	109	694	4644
ow-0438-04-001127	31.4950	336443	31.4477	33.6518	31.4439	33.6354	31.4912	33.6279	095	539	319	630	20384
ow-0438-05-001128	31.4419	337329	31.2973	33.7559	31.2836	33.6959	31.4282	33.6730	430	109	1115	442	228105
ow-0447-01-001152	32.7687	317987	32.7480	31.8020	32.7450	31.7885	32.7657	31.7852	1	902	101	977	7500
ow-0447-02-001153	32.7912	319593	32.7507	31.9657	32.7317	31.8796	32.7721	31.8732	062	22	257	500	93210
ow-0447-03-001154	32.7728	318173	32.7670	31.8182	32.7633	31.8015	32.7691	31.8005	1	799	29	892	2604
ow-0447-04-001155	32.7840	318726	32.7440	31.8790	32.7319	31.8244	32.7719	31.8180	6	493	199	796	58479
ow-0447-05-001156	32.7246	319242	32.7111	31.9264	32.7062	31.9042	32.7197	31.9020	336	267	401	390	7995
ow-0463-01-001189	33.4992	325301	33.2166	32.5710	33.1687	32.3412	33.4513	32.3003	1	197	1347	1474	1718842
ow-0463-02-001190	33.5066	325654	33.2281	32.6057	33.1786	32.3678	33.4570	32.3275	1	1	1327	1323	1752972
ow-0643-01-001540	32.9035	318446	32.9484	31.8515	32.9432	31.8758	32.8983	31.8689	123	1	339	136	29160
ow-0643-02-001541	32.9057	318665	32.9335	31.8708	32.9133	31.9652	32.8854	31.9610	155	117	289	640	70082
ow-0643-03-001542	32.9400	318755	32.9473	31.8767	32.9427	31.8985	32.9354	31.8974	324	137	359	258	4235
ow-0643-04-001543	32.9266	319080	32.9312	31.9087	32.9265	31.9309	32.9219	31.9302	294	322	316	445	2706
ow-0643-05-001544	32.9370	319609	32.9605	31.9645	32.9590	31.9717	32.9355	31.9681	395	597	508	637	4520
ow-0643-06-001545	32.9340	318996	32.9374	31.9001	32.9357	31.9079	32.9324	31.9074	320	271	336	314	688
ow-0643-07-001546	32.9215	319322	32.9231	31.9324	32.9218	31.9386	32.9202	31.9383	294	456	302	490	272
ow-0643-08-001547	32.9191	319372	32.9220	31.9377	32.9211	31.9420	32.9182	31.9416	288	485	302	509	336
ow-0643-09-001548	32.9164	319508	32.9247	31.9521	32.9232	31.9591	32.9149	31.9578	289	560	329	599	1560
ow-0643-10-001549	32.9188	319424	32.9213	31.9428	32.9196	31.9507	32.9171	31.9504	292	513	304	557	528

. YJY and SS jointly inspected the oil slicks in SAR scenes. YJY prepared the dataset and wrote the manuscripts. SS supported with his knowledge of SAR techniques. RG and FS contributed with valuable feedback on the explanations of oceanographic and atmospheric phenomena. All authors reviewed the manuscript.

. No potential conflict of interest was reported by the author(s).

. The dataset generation was partly funded by the DARTIS project, supported by the German Federal Ministry of Education and Research under grant number 03F0823B. The authors wish to thank Copernicus Programme for providing Sentinel-1 data, Copernicus Marine Service, and the other Earth observation data. The authors would also like to thank C. Pegel, C. Schnupfhagn, and D. Gnzel from the German Aerospace Center and P. Brandt from GEOMAR for their valuable feedback on the manuscripts. Additionally, the authors would like to thank the reviewers for their helpful comments.

References

Ahsbahs, T., Nygaard, N. G., Newcombe, A., and Badger, M.: Wind Farm Wakes from SAR and Doppler Radar, Remote Sensing, 12, https://doi.org/10.3390/rs12030462, 2020.

Alpers, W. and Huang, W.: On the Discrimination of Radar Signatures of Atmospheric Gravity Waves and Oceanic Internal Waves on Synthetic Aperture Radar Images of the Sea Surface, IEEE Transactions on Geoscience and Remote Sensing, 49, 1114–1126, https://doi.org/10.1109/TGRS.2010.2072930, 2011.

Alpers, W. and Zeng, K.: On Radar Signatures of Upwelling, Journal of Geodesy and Geoinformation Science, 4, 17, https://doi.org/10.11947/j.JGGS.2021.0102, 2021.

Alpers, W., Huang, W., and Xilin, G.: Observations of atmospheric gravity waves over the Chinese seas by spaceborne synthetic aperture radar, Proc. Dragon (ESA SP-655), 2008.

Alpers, W., Brandt, P., Lazar, A., Dagorne, D., Sow, B., Faye, S., Hansen, M. W., Rubino, A., Poulain, P.-M., and Brehmer, P.: A small-scale oceanic eddy off the coast of West Africa studied by multi-sensor satellite and surface drifter data, Remote Sensing of Environment, 129, 132–143, https://doi.org/10.1016/j.rse.2012.10.032, 2013.

Alpers, W., Dagorne, D., and Brandt, P.: Satellite Observations of Oceanic Eddies Around Africa, pp. 205–229, Springer Netherlands, Dordrecht, ISBN 978-94-017-8008-7, https://doi.org/10.1007/978-94-017-8008-7_11, 2014.

Alpers, W., Zhang, B., Mouche, A., Zeng, K., and Chan, P. W.: Rain footprints on C-band synthetic aperture radar images of the ocean - Revisited, Remote Sensing of Environment, 187, 169–185, https://doi.org/10.1016/j.rse.2016.10.015, 2016.

Alpers, W., Holt, B., and Zeng, K.: Oil spill detection by imaging radars: Challenges and pitfalls, Remote Sensing of Environment, 201, 133–147, https://doi.org/10.1016/j.rse.2017.09.002, 2017.

Amri, E., Dardouillet, P., Benoit, A., Courteille, H., Bolon, P., Dubucq, D., and Credoz, A.: Offshore Oil Slick Detection: From Photo-Interpreter to Explainable Multi-Modal Deep Learning Models Using SAR Images and Contextual Data, Remote Sensing, 14, https://doi.org/10.3390/rs14153565, 2022.

Atlas, D.: Origin of Storm Footprints on the Sea Seen by Synthetic Aperture Radar, Science, 266, 1364–1366, https://doi.org/10.1126/science.266.5189.1364, 1994.

Bakun, A. and Agostini, V. N.: Seasonal Patterns of Wind-Induced Upwelling/Downwelling in the Mediterranean Sea, Scientia Marina, 65, 243–257, https://doi.org/10.3989/scimar.2001.65n3243, 2001.

Berthon, J.-F. and Zibordi, G.: Bio-optical relationships for the northern Adriatic Sea, International Journal of Remote Sensing, 25, 1527–1532, https://doi.org/10.1080/01431160310001592544, 2004.

Brekke, C. and Solberg, A. H.: Oil spill detection by satellite remote sensing, Remote Sensing of Environment, 95, 1–13, https://doi.org/10.1016/j.rse.2004.11.015, 2005.

Brown, C. and Fingas, M.: A review of current global oil spill surveillance, monitoring and remote sensing capabilities, in: Proceedings of the Twenty-Eighth Arctic and Marine Oil Spill Program Technical Seminar. Environment Canada, Ottawa, Ontario, pp. 789–798, 2005.

Buongiorno Nardelli, B., Tronconi, C., Pisano, A., and Santoleri, R.: High and Ultra-High resolution processing of satellite Sea Surface Temperature data over Southern European Seas in the framework of MyOcean project, Remote Sensing of Environment, 129, 1–16, https://doi.org/10.1016/j.rse.2012.10.012, 2013.

Cantorna, D., Dafonte, C., Iglesias, A., and Arcay, B.: Oil spill segmentation in SAR images using convolutional neural networks. A comparative analysis with clustering and logistic regression algorithms, Applied Soft Computing, 84, 105 716, https://doi.org/10.1016/j.asoc.2019.105716, 2019.

Carpenter, A. and Kostianoy, A. G., eds.: Oil Pollution in the Mediterranean Sea: Part I: The International Context, The Handbook of Environmental Chemistry, Springer Cham, ISBN 978-3-030-12236-2, https://doi.org/10.1007/978-3-030-12236-2, 2016.

Chelton, D. B., Schlax, M. G., Samelson, R. M., and de Szoeke, R. A.: Global observations of large oceanic eddies, Geophysical Research Letters, 34, https://doi.org/10.1029/2007GL030812, 2007.

Chen, S., Wei, X., and Zheng, W.: ASA-DRNet: An Improved Deeplabv3+ Framework for SAR Image Segmentation, Electronics, 12, https://doi.org/10.3390/electronics12061300, 2023.

Chen, Y. and Wang, Z.: Marine Oil Spill Detection from SAR Images Based on Attention U-Net Model Using Polarimetric and Wind Speed Information, International Journal of Environmental Research and Public Health, 19, https://doi.org/10.3390/ijerph191912315, 2022.

Christiansen, M. B. and Hasager, C. B.: Wake effects of large offshore wind farms identified from satellite SAR, Remote Sensing of Environment, 98, 251–268, https://doi.org/10.1016/j.rse.2005.07.009, 2005.

Clemente-Colon, P. and Yan, X.-H.: Observations of East Coast upwelling conditions in synthetic aperture radar imagery, IEEE Transactions on Geoscience and Remote Sensing, 37, 2239–2248, https://doi.org/10.1109/36.789620, 1999.

Copeland, A., Ravichandran, G., and Trivedi, M.: Localized Radon transform-based detection of ship wakes in SAR images, IEEE Transactions on Geoscience and Remote Sensing, 33, 35–45, https://doi.org/10.1109/36.368224, 1995.

Danklmayer, A., Doring, B. J., Schwerdt, M., and Chandra, M.: Assessment of Atmospheric Propagation Effects in SAR Images, IEEE Transactions on Geoscience and Remote Sensing, 47, 3507–3518, https://doi.org/10.1109/TGRS.2009.2022271, 2009.

Deng, J., Dong, W., Socher, R., Li, L.-J., Li, K., and Fei-Fei, L.: ImageNet: A large-scale hierarchical image database, in: 2009 IEEE Conference on Computer Vision and Pattern Recognition, pp. 248–255, https://doi.org/10.1109/CVPR.2009.5206848, 2009.

Etling, D. and Brown, R. A.: Roll vortices in the planetary boundary layer: A review, Boundary-Layer Meteorology, 65, 215–248, https://doi.org/10.1007/BF00705527, 1993.

E.U. Copernicus Marine Service Information (CMEMS). Marine Data Store (MDS): Mediterranean Sea - High Resolution and Ultra High Resolution L3S Sea Surface Temperature, https://doi.org/10.48670/moi-00171, accessed: 2024-05-10, a.

E.U. Copernicus Marine Service Information (CMEMS). Marine Data Store (MDS): Mediterranean Sea, Bio-Geo-Chemical, L3, daily Satellite Observations (1997–ongoing), https://doi.org/10.48670/moi-00299, accessed: 2024-05-10, b.

E.U. Copernicus Marine Service Information (CMEMS). Marine Data Store (MDS): Global Ocean Hourly Sea Surface Wind and Stress from Scatterometer and Model, https://doi.org/10.48670/moi-00305, accessed: 2024-06-21, c.

European Space Agency: SNAP - ESA Sentinel Application Platform v8.0, http://step.esa.int, 2020.

Everingham, M., Van Gool, L., Williams, C. K., Winn, J., and Zisserman, A.: The PASCAL visual object classes (VOC) challenge, International journal of computer vision, 88, 303–338, https://doi.org/10.1007/s11263-009-0275-4, 2010.

Ferraro, G., Meyer-Roux, S., Muellenhoff, O., Pavliha, M., Svetak, J., Tarchi, D., and Topouzelis, K.: Long term monitoring of oil spills in European seas, International Journal of Remote Sensing, 30, 627–645, https://doi.org/10.1080/01431160802339464, 2009.

Fingas, M. and Brown, C.: Chapter 5 - Oil Spill Remote Sensing, in: Oil Spill Science and Technology (Second Edition), edited by Fingas, M., pp. 305–385, Gulf Professional Publishing, Boston, second edition edn., ISBN 978-0-12-809413-6, https://doi.org/10.1016/B978-0-12-809413-6.00005-9, 2017.

Franceschi, N., Recchia, A., Piantanida, R., Giudici, D., Albinet, C., and Miranda, N.: A Global C-Band RFI Monitoring System Based on Sentinel-1 Data, in: 2021 IEEE International Geoscience and Remote Sensing Symposium IGARSS, pp. 1658–1661, https://doi.org/10.1109/IGARSS47720.2021.9554119, 2021.

Franceschi, N., Recchia, A., Piantanida, R., Hajduch, G., Vincent, P., Pinheiro, M., Miranda, N., and Albinet, C.: Operational RFI Mitigation Approach in Sentinel-1 IPF, in: EUSAR 2022; 14th European Conference on Synthetic Aperture Radar, pp. 1–5, 2022.

Gade, M., Scholz, J., and von Viebahn, C.: On the detectability of marine oil pollution in European marginal waters by means of ERS SAR imagery, in: IGARSS 2000. IEEE 2000 International Geoscience and Remote Sensing Symposium. Taking the Pulse of the Planet: The Role of Remote Sensing in Managing the Environment. Proceedings (Cat. No.00CH37120), vol. 6, pp. 2510–2512 vol.6, https://doi.org/10.1109/IGARSS.2000.859623, 2000.

Gade, M., Byfield, V., Ermakov, S., Lavrova, O., and Mitnik, L.: Slicks as Indicators for Marine Processes, Oceanography (Washington D.C.), 26, 138–149, 2013.

GEBCO Bathymetric Compilation Group 2023: The GEBCO_2023 Grid - a continuous terrain model of the global oceans and land, https://www.gebco.net/, https://doi.org/10.5285/f98b053b-0cbc-6c23-e053-6c86abc0af7b, accessed: 2024-06-21, 2023.

Gertman, I., Zodiatis, G., Murashkovsky, A., Hayes, D., and Brenner, S.: Determination of the locations of southeastern Levantine anticyclonic eddies from CTD data, Rapp. Commun. Int. Mer. Mediterr, 38, 151, 2007.

Graziano, M. D., Grasso, M., and D'Errico, M.: Performance Analysis of Ship Wake Detection on Sentinel-1 SAR Images, Remote Sensing, 9, https://doi.org/10.3390/rs9111107, 2017.

Hajduch, G., Franceschi, N., Pinheiro, M., and Valentino, A.: SAR-MPC Sentinel-1: Using the RFI annotations, https://doi.org/10.13140/RG.2.2.13758.56641, 2022.

Hasimoto-Beltran, R., Canul-Ku, M., Díaz Méndez, G. M., Ocampo-Torres, F. J., and Esquivel-Trava, B.: Ocean oil spill detection from SAR images based on multi-channel deep learning semantic segmentation, Marine Pollution Bulletin, 188, 114 651, https://doi.org/10.1016/j.marpolbul.2023.114651, 2023.

Karathanassi, V., Topouzelis, K., Pavlakis, P., and Rokos, D.: An object-oriented methodology to detect oil spills, International Journal of Remote Sensing, 27, 5235–5251, https://doi.org/10.1080/01431160600693575, 2006.

Karimova, S. and Gade, M.: Submesoscale eddies seen by spaceborne radar, Proc. EMEC, pp. 665–676, 2013.

Karin, T.: toddkarin/global-land-mask: Release of version 1.0.0, https://doi.org/10.5281/zenodo.4066722, 2020.

Knauss, J. A. and Garfield, N.: Introduction to physical oceanography, Waveland Press, 2016.

Konik, M. and Bradtke, K.: Object-oriented approach to oil spill detection using ENVISAT ASAR images, ISPRS Journal of Photogrammetry and Remote Sensing, 118, 37–52, https://doi.org/10.1016/j.isprsjprs.2016.04.006, 2016.

Krestenitis, M., Orfanidis, G., Ioannidis, K., Avgerinakis, K., Vrochidis, S., and Kompatsiaris, I.: Oil Spill Identification from Satellite Images Using Deep Neural Networks, Remote Sensing, 11, https://doi.org/10.3390/rs11151762, 2019.

Langmuir, I.: Surface Motion of Water Induced by Wind, Science, 87, 119–123, https://doi.org/10.1126/science.87.2250.119, 1938.

Lehner, S., Horstmann, J., Koch, W., and Rosenthal, W.: Mesoscale wind measurements using recalibrated ERS SAR images, Journal of Geophysical Research: Oceans, 103, 7847–7856, https://doi.org/10.1029/97JC02726, 1998.

Li, X.: Atmospheric vortex streets and gravity waves, pp. 341–354, National Oceanic and Atmospheric Administration, Washington, DC, USA, 2004.

Li, X. and Lehner, S.: Observation of TerraSAR-X for Studies on Offshore Wind Turbine Wake in Near and Far Fields, IEEE Journal of Selected Topics in Applied Earth Observations and Remote Sensing, 6, 1757–1768, https://doi.org/10.1109/JSTARS.2013.2263577, 2013.

Lin, I.-I., Alpers, W., Khoo, V., Lim, H., Lim, T., and Kasilingam, D.: An ERS-1 synthetic aperture radar image of a tropical squall line compared with weather radar data, IEEE Transactions on Geoscience and Remote Sensing, 39, 937–945, https://doi.org/10.1109/36.921411, 2001.

Liu, A. K., Chang, Y. S., Hsu, M.-K., and Liang, N. K.: Evolution of nonlinear internal waves in the East and South China Seas, Journal of Geophysical Research: Oceans, 103, 7995–8008, https://doi.org/10.1029/97JC01918, 1998.

Liu, G., Perrie, W., Kudryavtsev, V., He, Y., Shen, H., Zhang, B., and Hu, H.: Radar imaging of intense nonlinear Ekman divergence, Geophysical Research Letters, 43, 9810–9818, https://doi.org/10.1002/2016GL070799, 2016.

Lloyd, S.: Least squares quantization in PCM, IEEE Transactions on Information Theory, 28, 129–137, https://doi.org/10.1109/TIT.1982.1056489, 1982.

Lyden, J. D., Hammond, R. R., Lyzenga, D. R., and Shuchman, R. A.: Synthetic aperture radar imaging of surface ship wakes, Journal of Geophysical Research: Oceans, 93, 12 293–12 303, https://doi.org/10.1029/JC093iC10p12293, 1988.

Lévy, M., Ferrari, R., Franks, P. J. S., Martin, A. P., and Rivière, P.: Bringing physics to life at the submesoscale, Geophysical Research Letters, 39, https://doi.org/10.1029/2012GL052756, 2012.

MacQueen, J.: Some methods for classification and analysis of multivariate observations, in: Proceedings of the fifth Berkeley symposium on mathematical statistics and probability, vol. 1, pp. 281–297, Oakland, CA, USA, 1967.

Mahmoud, A. S., Mohamed, S. A., El-Khoriby, R. A., AbdelSalam, H. M., and El-Khodary, I. A.: Oil spill identification based on dual attention UNet model using Synthetic Aperture Radar images, Journal of the Indian Society of Remote Sensing, 51, 121–133, 2023.

McWilliams, J. C. and Molemaker, M. J.: Baroclinic Frontal Arrest: A Sequel to Unstable Frontogenesis, Journal of Physical Oceanography, 41, 601–619, https://doi.org/10.1175/2010JPO4493.1, 2011.

Menna, M., Poulain, P.-M., Zodiatis, G., and Gertman, I.: On the surface circulation of the Levantine sub-basin derived from Lagrangian drifters and satellite altimetry data, Deep Sea Research Part I: Oceanographic Research Papers, 65, 46–58, https://doi.org/10.1016/j.dsr.2012.02.008, 2012.

Meyer, F. J., Nicoll, J. B., and Doulgeris, A. P.: Correction and Characterization of Radio Frequency Interference Signatures in L-Band Synthetic Aperture Radar Data, IEEE Transactions on Geoscience and Remote Sensing, 51, 4961–4972, https://doi.org/10.1109/TGRS.2013.2252469, 2013.

Miller, T., Potter, L., and McCorkle, J.: RFI suppression for ultra wideband radar, IEEE Transactions on Aerospace and Electronic Systems, 33, 1142–1156, https://doi.org/10.1109/7.625096, 1997.

Ministry of Transport and Road Safety, Israel: Israel Meteorological Service, https://ims.gov.il/en/data_gov, accessed: 2024-07-31.

Monti-Guarnieri, A., Giudici, D., and Recchia, A.: Identification of C-Band Radio Frequency Interferences from Sentinel-1 Data, Remote Sensing, 9, https://doi.org/10.3390/rs9111183, 2017.

Natsuaki, R., Motohka, T., Watanabe, M., Shimada, M., and Suzuki, S.: An Autocorrelation-Based Radio Frequency Interference Detection and Removal Method in Azimuth-Frequency Domain for SAR Image, IEEE Journal of Selected Topics in Applied Earth Observations and Remote Sensing, 10, 5736–5751, https://doi.org/10.1109/JSTARS.2017.2775205, 2017.

Nieto-Hidalgo, M., Gallego, A.-J., Gil, P., and Pertusa, A.: Two-Stage Convolutional Neural Network for Ship and Spill Detection Using SLAR Images, IEEE Transactions on Geoscience and Remote Sensing, 56, 5217–5230, https://doi.org/10.1109/TGRS.2018.2812619, 2018.

Pegliasco, C., Chaigneau, A., Morrow, R., and Dumas, F.: Detection and tracking of mesoscale eddies in the Mediterranean Sea: A comparison between the Sea Level Anomaly and the Absolute Dynamic Topography fields, Advances in Space Research, 68, 401–419, https://doi.org/10.1016/j.asr.2020.03.039, 25 Years of Progress in Radar Altimetry, 2021.

Qi, L., Wang, M., Hu, C., and Holt, B.: On the capacity of Sentinel-1 synthetic aperture radar in detecting floating macroalgae and other floating matters, Remote Sensing of Environment, 280, 113 188, https://doi.org/https://doi.org/10.1016/j.rse.2022.113188, 2022.

Rey, M., Tunaley, J., Folinsbee, J., Jahans, P., Dixon, J., and Vant, M.: Application Of Radon Transform Techniques to Wake Detection in Seasat-A SAR Images, IEEE Transactions on Geoscience and Remote Sensing, 28, 553–560, https://doi.org/10.1109/TGRS.1990.572948, 1990.

Robinson, A. R.: Overview and Summary of Eddy Science, in: Eddies in Marine Science, edited by Robinson, A. R., pp. 3–15, Springer Berlin Heidelberg, Berlin, Heidelberg, ISBN 978-3-642-69003-7, https://doi.org/10.1007/978-3-642-69003-7_1, 1983.

Robinson, I. S.: Measuring the Oceans from Space: the Principles and Methods of Satellite Oceanography, Springer Science & Business Media, ISBN 978-3-540-42647-9, 2004.

Robinson, I. S.: Discovering the ocean from space: the unique applications of satellite oceanography, Springer Science & Business Media, ISBN 978-3-540-24430-1, https://doi.org/10.1007/978-3-540-68322-3, 2010.

Rosen, P. A., Hensley, S., and Le, C.: Observations and mitigation of RFI in ALOS PALSAR SAR data: Implications for the DESDynI mission, in: 2008 IEEE Radar Conference, pp. 1–6, https://doi.org/10.1109/RADAR.2008.4720738, 2008.

Shemdin, O. H.: Synthetic aperture radar imaging of ship wakes in the Gulf of Alaska, Journal of Geophysical Research: Oceans, 95, 16 319–16 338, https://doi.org/10.1029/JC095iC09p16319, 1990.

Siokou-Frangou, I., Christaki, U., Mazzocchi, M. G., Montresor, M., Ribera d'Alcalá, M., Vaqué, D., and Zingone, A.: Plankton in the open Mediterranean Sea: a review, Biogeosciences, 7, 1543–1586, https://doi.org/10.5194/bg-7-1543-2010, 2010.

Stevens, J.: NASA Earth Observatory Map, https://visibleearth.nasa.gov/images/147190/explorer-base-map, Accessed: 2020-09-08, 2020.

Szegedy, C., Vanhoucke, V., Ioffe, S., Shlens, J., and Wojna, Z.: Rethinking the Inception Architecture for Computer Vision, CoRR, abs/1512.00567, http://arxiv.org/abs/1512.00567, 2015.

Tings, B., Pleskachevsky, A., and Wiehle, S.: Comparison of detectability of ship wake components between C-Band and X-Band synthetic aperture radar sensors operating under different slant ranges, ISPRS Journal of Photogrammetry and Remote Sensing, 196, 306–324, https://doi.org/10.1016/j.isprsjprs.2022.12.008, 2023.

Topouzelis, K. and Psyllos, A.: Oil spill feature selection and classification using decision tree forest on SAR image data, ISPRS Journal of Photogrammetry and Remote Sensing, 68, 135–143, https://doi.org/10.1016/j.isprsjprs.2012.01.005, 2012.

Trujillo-Acatitla, R., Tuxpan-Vargas, J., Ovando-Vázquez, C., and Monterrubio-Martínez, E.: Marine oil spill detection and segmentation in SAR data with two steps Deep Learning framework, Marine Pollution Bulletin, 204, 116 549, https://doi.org/10.1016/j.marpolbul.2024.116549, 2024.

Tzutalin: LabelImg, https://github.com/tzutalin/labelImg, 2015.

Volpe, G., Colella, S., Brando, V. E., Forneris, V., La Padula, F., Di Cicco, A., Sammartino, M., Bracaglia, M., Artuso, F., and Santoleri, R.: Mediterranean ocean colour Level 3 operational multi-sensor processing, Ocean Science, 15, 127–146, 2019.

von Jackowski, A., Bouchachi, N., Barral, Q.-B., Labatut, P., Marie, B., Crispi, O., Escoubeyrou, K., Paulin, C.-H., Dimier, C., Ras, J., et al.: Seasonality of amino acid enantiomers and microbial communities at MOLA time series in the NW Mediterranean Sea, Organic Geochemistry, 196, 104 839, 2024.

Wessel, P. and Smith, W. H. F.: A global, self-consistent, hierarchical, high-resolution shoreline database, Journal of Geophysical Research: Solid Earth, 101, 8741–8743, https://doi.org/10.1029/96JB00104, 1996.

Woodhouse, I. H.: Introduction to Microwave Remote Sensing, CRC press, 2006.

Yang, Y.-J. and Schnupfhagn, C.: A near real-time automated oil spill monitoring system using SAR imagery from the European Copernicus mission, in: Active and Passive Remote Sensing of Oceans, Seas, and Lakes, edited by Frouin, R. J., Murakami, H., Choi, J.-K., and Tseng, K.-H., vol. 13264, p. 132640G, International Society for Optics and Photonics, SPIE, https://doi.org/10.1117/12.3040472, 2025.

Yang, Y.-J. and Singha, S.: Oil Slicks, Look-Alikes and Other Remarkable SAR Signatures in Sentinel-1 Imagery in the Eastern Mediterranean Sea in 2019, PANGAEA, https://doi.org/10.1594/PANGAEA.980773, 2025.

Yang, Y.-J., Singha, S., and Goldman, R.: A Near Real-Time Automated Oil Spill Detection and Early Warning System Using Sentinel-1 SAR Imagery for the Southeastern Mediterranean Sea, International Journal of Remote Sensing, 45, 1997–2027, https://doi.org/10.1080/01431161.2024.2321468, 2024.

Zeng, K. and Wang, Y.: A Deep Convolutional Neural Network for Oil Spill Detection from Spaceborne SAR Images, Remote Sensing, 12, https://doi.org/10.3390/rs12061015, 2020.

Zhou, L., Zheng, G., Wang, C., Shao, J., Chen, P., Ren, L., Wan, X., Zhu, Y., and Wang, H.: Wavelength Extraction and Analysis of Wind Streaks in SAR Imagery, IEEE Journal of Selected Topics in Applied Earth Observations and Remote Sensing, 18, 16 769–16 779, https://doi.org/10.1109/JSTARS.2025.3584105, 2025.

Zodiatis, G., Drakopoulos, P., Brenner, S., and Groom, S.: Variability of the Cyprus warm core Eddy during the CYCLOPS project, Deep Sea Research Part II: Topical Studies in Oceanography, 52, 2897–2910, https://doi.org/10.1016/j.dsr2.2005.08.020, on the Nature of Phosphorus Cycling and Limitation in the Eastern Mediterranean, 2005.